



# CO<sub>2</sub>-derived edge-boron-doped hierarchical porous carbon catalysts for highly effective electrochemical H<sub>2</sub>O<sub>2</sub> production

Ayeong Byeon <sup>a</sup>, Jae Won Choi <sup>b</sup>, Hong Woo Lee <sup>c</sup>, Won Chan Yun <sup>a</sup>, Wenjun Zhang <sup>b,d</sup>, Chang-Kyu Hwang <sup>b</sup>, Seung Yong Lee <sup>b</sup>, Sang Soo Han <sup>c,\*</sup>, Jong Min Kim <sup>b,d,e,\*\*</sup>, Jae W. Lee <sup>a,\*</sup>

<sup>a</sup> Department of Chemical and Biomolecular Engineering, Korea Advanced Institute of Science and Technology, 291 Daehak-ro, Yuseong-gu, Daejeon 34141, Republic of Korea

<sup>b</sup> Materials Architecturing Research Center, Korea Institute of Science and Technology, 14-gil 5 Hwarang-ro, Seongbuk-gu, Seoul 02792, Republic of Korea

<sup>c</sup> Computational Science Research Center, Korea Institute of Science and Technology, 14-gil 5 Hwarang-ro, Seongbuk-gu, Seoul 02792, Republic of Korea

<sup>d</sup> Division of Nano & Material Technology, University of Science and Technology (UST), Daejeon 34113, South Korea

<sup>e</sup> KHU-KIST Department of Converging Science and Technology, Kyung Hee University, Seoul 02447, Republic of Korea



## ARTICLE INFO

### Keywords:

CO<sub>2</sub>-derived porous carbon  
Edge-boron doping  
Hydrogen peroxide production  
Oxygen reduction reaction  
Flow reactor

## ABSTRACT

Electrochemical hydrogen peroxide (H<sub>2</sub>O<sub>2</sub>) synthesis via the two-electron oxygen reduction reaction (2e<sup>-</sup> ORR) is considered a promising alternative to the anthraquinone process due to its eco-friendliness and on-site production. Recently, although B-doped carbon (BC) has been suggested as a promising 2e<sup>-</sup> ORR catalyst, the question of whether BC can further improve catalytic activity by tuning the doping configuration and site still remains unanswered. This work demonstrates CO<sub>2</sub>-derived edge-B-doped porous carbon (E-BPC) for highly effective electrochemical H<sub>2</sub>O<sub>2</sub> production. Herein, it is revealed that the oxygenated B-doping configurations (BCO<sub>2</sub> and BC<sub>2</sub>O) at edge sites are responsible for enhanced 2e<sup>-</sup> ORR activity and stability. Outstanding mass activity (54.7 A g<sup>-1</sup> at 0.65 V vs. RHE) is demonstrated with the highest high production rate in a flow reactor among the reported studies, of 24.3 mol g<sub>cat</sub><sup>-1</sup> h<sup>-1</sup>. The faradaic efficiency of the E-BPC was maintained (~82%) for over 100 h without performance degradation.

## 1. Introduction

The energy-efficient and environmentally-benign production of chemicals is of prime interest since it has the potential to reduce CO<sub>2</sub> emissions and minimize impacts on ecosystems [1–4]. The electrochemical production of hydrogen peroxide (H<sub>2</sub>O<sub>2</sub>) is a good example of such sustainable methods [5,6]. H<sub>2</sub>O<sub>2</sub> has been used in a variety of applications including the pulp and paper, semiconductor, water treatment and disinfection industries because of its strong oxidizing property [7–9]. To meet the increasing global demand, most H<sub>2</sub>O<sub>2</sub> is currently produced using the anthraquinone process. However, its pathway is inherently complicated and requires high energy consumption with a large amount of hydrogen, and expensive palladium catalysts [10,11]. In addition, this process relies on a centralized infrastructure and requires the expensive transport and storage of explosive concentrated H<sub>2</sub>O<sub>2</sub> solutions [12,13].

To tackle these issues, electrochemical H<sub>2</sub>O<sub>2</sub> production has been proposed, and has recently attracted attention as an alternative process because it is safe, environmental-friendly, and capable of on-site production [2,14]. Electrochemical H<sub>2</sub>O<sub>2</sub> production via the two-electron (2e<sup>-</sup>) oxygen reduction reaction (ORR) is a green route for the electrocatalytic synthesis of H<sub>2</sub>O<sub>2</sub> under mild conditions (e.g., at room temperature and ambient pressure with an aqueous electrolyte) without organic additives and high-purity H<sub>2</sub> gas [15–20]. So far, most studies on ORR catalysts have focused on the development of high-performance catalysts for the 4e<sup>-</sup> ORR to improve the cell performance of fuel cells [3,21–23]. However, to synthesize H<sub>2</sub>O<sub>2</sub>, it is more important to develop highly active and selective catalysts toward the 2e<sup>-</sup> ORR.

Noble metals and their alloys (e.g., Pd, Au, and Pt-Hg) have demonstrated high selectivity for the 2e<sup>-</sup> ORR [24–28], however, using expensive noble metals is difficult to implement on a large scale. More practically, carbon-based materials with oxygen functional groups (e.g.,

\* Corresponding authors.

\*\* Corresponding author at: Materials Architecturing Research Center, Korea Institute of Science and Technology, 14-gil 5 Hwarang-ro, Seongbuk-gu, Seoul 02792, Republic of Korea.

E-mail addresses: [sangsoo@kist.re.kr](mailto:sangsoo@kist.re.kr) (S.S. Han), [jongminkim@kist.re.kr](mailto:jongminkim@kist.re.kr) (J.M. Kim), [jaewlee@kaist.ac.kr](mailto:jaewlee@kaist.ac.kr) (J.W. Lee).

oxidized carbon nanotube [29], graphene oxide [30], and defective carbon [31] have been suggested as highly selective electrocatalysts for the  $2e^-$  ORR. Even though these state-of-the-art oxidized carbon catalysts demonstrated great selectivity for the  $2e^-$  ORR, they've suffered significant overpotentials when delivering large current densities due to their high charge transfer resistance, resulting from surface oxidation. Highly active and selective boron (B)-doped carbon was recently employed for the  $2e^-$  ORR to overcome the activity-selectivity dilemma of oxidized carbon materials, and this prior study demonstrated the great potential of B-doped carbon catalysts for practical electrochemical  $H_2O_2$  synthesis under industrially-relevant currents (up to  $300 \text{ mA cm}^{-2}$ ) [32].

Even though they determined the best B dopant among nonmetal elements (e.g., B, N, P, and S) instead of oxygen (O) dopant for the  $2e^-$  ORR, only the  $BC_3$  doping configuration located in the basal plane was reported as the active site. That is, the effect of B-doping of the edge defect sites of the carbon was not studied. In this regard, It is known that heteroatom doping of edge sites (e.g., zigzag and armchair) in carbon materials can significantly change the electron distribution of carbon atoms, affecting their physical and chemical properties [33,34]. Therefore, to realize further improvements in  $2e^-$  ORR activity, it is crucial to investigate the effect of B-doping on the edge defect sites, beyond the doping of the basal plane. Moreover, active-B-C configurations of  $B_4C$ ,  $BC_3$ ,  $BCO_2$  and  $BC_2O$  for the  $2e^-$  ORR have been reported [35], however their activities were also investigated with active B-C configurations located in the basal plane. In other word, the  $2e^-$  ORR activity of various B-doping configurations at the edge site have not yet been studied. Considering these points, there are still questions about utilizing edge as a doping site for further performance improvement of B-doped carbon catalysts that can overcome the activity-selectivity dilemma.

Herein, we report a highly active and selective  $CO_2$ -derived edge-B-doped porous carbon (E-BPC) catalyst for electrochemical  $H_2O_2$  production through the  $2e^-$  ORR process. To synthesize E-BPC, we adopted a  $CO_2$  conversion process based on  $CO_2$  gas and sodium borohydride ( $NaBH_4$ ) as a reducing agent [36,37]. This  $CO_2$  conversion process based on  $NaBH_4$  has significant advantages, as follows. 1) It enables a wide range of B-doping concentrations (up to 16 at%), large surface area ( $\sim 800 \text{ m}^2 \text{ g}^{-1}$ ) and hierarchical porous structure; 2) requires mild synthesis conditions (e.g., 1 atm and  $500\text{--}700^\circ\text{C}$ ), compared to other high-temperature carbon synthesis, which are more than  $800^\circ\text{C}$  [38–40], and 3) also produces valuable products (i.e., electrocatalysts) through utilization of a greenhouse gas,  $CO_2$ .

First, pristine B-doped carbon (BC) was synthesized from  $CO_2$  conversion using  $NaBH_4$ , and B-doped porous carbon (BPC) was obtained through the combined procedure of  $CO_2$  conversion and further surface activation under  $CO_2$  gas, to maximize the catalytic surface area and expand the edge defect sites. After that, by additional B-doping of the edge sites of the BPC by annealing BPC with boric acid, E-BPC was finally obtained. The material characterizations revealed that E-BPC has a hierarchical pore structure favorable for the enhanced mass transport of reactant and product, which promotes the  $2e^-$  ORR. Furthermore, regarding the chemical configuration of B-C on the surface, as evidenced by XPS analysis, the portion of  $BC_3$ ,  $BC_2O$ , and  $BCO_2$  was increased significantly, from 49.9% for BC to 62.6% and 78.3% for BPC and E-BPC, respectively.

In order to more clearly understand the effect of B-doping of each site on electrocatalytic performance, we also carried out density functional theory (DFT) calculations. From the results, the doping configurations of the edge sites ( $BC_2O$  at the armchair edge site,  $BCO_2$  at the zigzag edge site) were newly identified as highly active sites for the  $2e^-$  ORR, in addition to the previously known  $BC_3$  in the basal plane.

Consequently, using a liquid half-cell test, the top-performing E-BPC catalyst was demonstrated to have high selectivity of  $> 80\%$ , as well as excellent mass activity ( $54.7 \text{ A g}^{-1}$  at  $0.65 \text{ V}$  vs. RHE). This excellent mass activity is the best value among the reported metal-free electrocatalysts for the  $2e^-$  ORR. In addition, the E-BPC catalyst was found to

have  $84 \text{ mV}$  overpotential at  $300 \text{ mA cm}^{-2}$ , which is much lower than the  $232 \text{ mV}$  overpotential of the pristine  $CO_2$ -derived B-doped carbon (BC). It also demonstrated impressive  $H_2O_2$  productivity of  $24.3 \text{ mol g}_{cat}^{-1} \text{ h}^{-1}$  in a flow reactor system which surpasses that of state-of-the-art electrocatalysts for the  $2e^-$  ORR.

## 2. Experimental

### 2.1. Materials

Argon (Ar,  $> 99.9\%$ ) and carbon dioxide ( $CO_2$ ,  $> 99.9\%$ ) were purchased from Deokyang Co., Ltd. Sodium borohydride ( $NaBH_4$ ,  $> 99\%$ ), and boric acid ( $H_3BO_3$ ,  $> 99.5\%$ ) were purchased from Samchun. Hydrochloric acid (HCl, 37 wt% in water) was obtained from Junsei Chemical Co., Ltd. All of the chemicals were used without further purification. Ammonia solution ( $NH_4OH$ , 25–30%) was purchased from Samchun.

### 2.2. Synthesis of BC

The BC sample was synthesized from the reaction of  $NaBH_4$  and  $CO_2$  at  $500^\circ\text{C}$ . The ramping rate to  $500^\circ\text{C}$  was  $5^\circ\text{C min}^{-1}$  and the temperature was maintained for 2 hrs under 70 sccm of  $CO_2$  flow. After the reaction was complete, the black residue was washed with 5 M HCl overnight at room temperature. And it was then washed thoroughly with DIW, and dried in a vacuum oven at  $80^\circ\text{C}$ .

### 2.3. Synthesis of BPC

The BPC was synthesized as follows. The  $CO_2$  conversion was carried out with heat treatment of  $NaBH_4$  at  $700^\circ\text{C}$ . The ramping rate to  $700^\circ\text{C}$  was  $5^\circ\text{C min}^{-1}$ , and the reaction proceeded at a reaction temperature of  $700^\circ\text{C}$  for 2 hrs under 70 sccm of  $CO_2$  flow. After the reaction was complete, the black residue was washed with 5 M HCl overnight at room temperature. Then it was washed thoroughly with water, and dried in a vacuum oven at  $80^\circ\text{C}$ . The resultant carbon material was named BPC.

### 2.4. Synthesis of E-BPC

The E-BPC was synthesized as follows. 0.2 g of BPC was mixed mechanically with 2 g of boric acid and the mixed powder was heat treated up to  $800^\circ\text{C}$  ( $5^\circ\text{C min}^{-1}$ ) for 2 hrs under 40 sccm of Ar. The obtained powder was washed with hot DIW for 3 hrs, filtered and dried overnight in a vacuum oven at  $80^\circ\text{C}$ . The resultant carbon material was named as E-BPC.

### 2.5. Materials characterization

The X-ray diffraction (XRD) spectra were measured with a Dmax2500/PC (Rigaku) using Cu K $\alpha$  as the radiation source. The Raman spectra and mapping data were taken by In Via Raman Microscope (Renishaw) with a 532 nm Nd:Yag laser. The Raman mapping images were acquired with  $20 \mu\text{m} \times 20 \mu\text{m}$  and the spot size was  $0.3 \mu\text{m}$ . The X-ray photoelectron spectroscopy (XPS) data was provided by K-alpha (Thermo VG Scientific, America) with Al (1386.7 eV) as a X-ray source. Near edge X-ray absorption fine structure (NEXAFS) measurements for B K-edge was performed at 1D XAS KIST-PAL beamline of Pohang Accelerator Laboratory in South Korea. Time of flight secondary ion mass spectrometry (ToF-SIMS) was analyzed using an ION-TOF GmbH TOF-SIMS5 equipped with a Bi metal ion source.

Brunauer-Emmett-Teller (BET) surface area was determined by  $N_2$  adsorption-desorption isotherms at  $77 \text{ K}$  from TriStar II 3020 (Micrometrics). The pore size distribution was derived from the BJH theory. The micropore volume ( $V_{micro}$ ) was determined with the t-plot method. The morphology of porous carbons and electrode structure in flow cell setup were observed by the field emission scanning electron microscopy

(Regulus 8230, Hitachi). The transmission electron microscopy (TEM) images and electron energy loss spectroscopy (EELS) were obtained by a Cs-corrected microscope Titan<sup>TM</sup> 80–300 (FEI) equipped with a GATAN Quantum 966 spectrometer. Attenuated total reflection Fourier transform infrared (ATR-FTIR) spectra were recorded using a Bruker Alpha-Pa spectrometer (Bruker Optik GmbH) at a resolution of 2 cm<sup>-1</sup> from 500 to 4000 cm<sup>-1</sup>. Gas concentration profiles were obtained by monitoring the outlet gas from the furnace using a quadrupole mass spectrometer (QMS 200, Pfeiffer Vacuum). The mixed gas consisting of 15% of CO<sub>2</sub>, 80% of N<sub>2</sub>, and 5% of O<sub>2</sub> were utilized for this experiment. The 2 g of NaBH<sub>4</sub> powder were loaded into the alumina crucible inside the furnace and the ramping rate to 500 °C was 5 °C min<sup>-1</sup> and maintained at the temperature for 2 hrs.

## 2.6. Rotating ring disk electrode (RRDE) measurement

The electrochemical measurements were performed using an Autolab PGSTAT302N-potentiostat. The rotating ring disk electrode measurements were conducted in a three-electrode system with a RRDE (Glassy carbon electrode and a Pt ring electrode), a Ag/AgCl reference electrode, and a Pt plate counter electrode. For the accurate measurement of RRDE test, the collection efficiency (N) was experimentally determined to be 0.25 in the ferrocyanide/ferricyanide half reaction system. The catalyst ink was prepared by mixing 3 mg of catalyst in 50 μL of 5% Nafion solution, 100 μL of deionized water, and 1.8 mL of ethanol. Then, the ink was homogeneously dispersed by ultrasonication for 30 min and 3.92 μL of ink was drop-casted on the glassy carbon electrode (0.196 cm<sup>2</sup> area) and dried under an infrared lamp. Prior to ORR measurement, cyclic voltammetry (CV) was performed at a scan rate of 100 mV s<sup>-1</sup> for 10 cycles between 0.05 and 1 V vs. RHE for the disk electrode and at a scan rate of 500 mV s<sup>-1</sup> for 20 cycles at the same potential range for the Pt ring cleaning in Ar-saturated 0.1 M KOH solution and 0.1 M Na<sub>2</sub>SO<sub>4</sub>. To obtain background current, polarization curves in the Ar-saturated electrolyte were obtained using linear sweep voltammetry (LSV) from 0.05 to 1 V vs. RHE at a rotation speed of 1600 rpm with a fixed potential of Pt ring at 1.2 V vs. RHE. Then, O<sub>2</sub> gas was purged for at least 5 min, and the polarization curves in O<sub>2</sub>-saturated 0.1 M KOH were measured under the same condition as above. The subtraction of background current in Ar-saturated electrolyte from that in O<sub>2</sub>-saturated electrolyte determines the ORR current. The H<sub>2</sub>O<sub>2</sub> selectivity and faradaic efficiency were calculated using the following equation:

$$\text{Selectivity of H}_2\text{O}_2(\%) = 200 \times \frac{I_r/N}{I_d + I_r/N} \quad (1)$$

$$\text{Faradaic efficiency of H}_2\text{O}_2(\%) = 100 \times \frac{I_r/N}{I_d} \quad (2)$$

where  $I_d$  and  $I_r$  are the disk and ring current, respectively. The electron transfer number (n) was calculated by the equation:

$$n = \frac{4 \times I_d}{I_d + I_r/N} \quad (3)$$

The kinetic current ( $I_k$ ) was derived by correcting the loss from mass transport as follows:

$$\frac{1}{I_m} = \frac{1}{I_k} + \frac{1}{I_l} \quad (4)$$

where  $I_m$  and  $I_l$  indicate the measured total current on the disk and diffusion-limited current.

In general, the highest current value in the measured potential range is determined as diffusion-limited current, but for more accurate calculation, we used  $I_l$  calculated from the Levich equation as follows:

$$I_l = 0.62nFAD_0^{2/3}\omega^{1/2}\nu^{-1/6}C_0 \quad (5)$$

where  $F$ ,  $A$ ,  $D_0$ ,  $\omega$ ,  $\nu$ , and  $C_0$  correspond to the Faradaic constant (96,485 C mol<sup>-1</sup>), disk electrode area (0.196 cm<sup>2</sup>), diffusion coefficient of O<sub>2</sub> (1.85 × 10<sup>-5</sup> cm<sup>2</sup> s<sup>-1</sup>), electrode rotation speed (in rad s<sup>-1</sup>), kinematic viscosity of O<sub>2</sub> (0.89 × 10<sup>-2</sup> cm<sup>2</sup> s<sup>-1</sup>), and O<sub>2</sub> concentration (1.21 × 10<sup>-6</sup> mol cm<sup>-3</sup>). Mass activity was calculated by dividing the ring current density at 0.65 and 0.75 V vs. RHE by mass loading of the catalyst.

## 2.7. Three-electrode flow cell measurement

To demonstrate the performance of the catalyst at a large-scale current density, the electrochemical ORR was measured in a three-electrode flow cell system. For working electrode preparation, 4 mg of catalyst was dispersed in 67 μL of 5% Nafion solution and 4 mL of ethanol with ultrasonication for 30 min. The catalyst ink was spray-coated on a gas diffusion layer (GDL) electrode (Sigracet 39 BB) with a microporous layer (MPL). The mass loading of the electrode was 0.25–0.5 mg cm<sup>-2</sup>. A Hg/HgO electrode and NiFeMo foil were used as a reference and a counter electrode, respectively, and anion exchange membrane (FAA-3-PK-130, Fumatech) was employed as a separator. 40 mL of 1 M KOH solution and 1 M Na<sub>2</sub>SO<sub>4</sub> was circulated through the flow cell and reservoir using a peristaltic pump at a flow rate of 40 mL min<sup>-1</sup> to each of the cathode and anode. A flow rate of O<sub>2</sub> gas was fixed at 20 sccm. I-V curves were obtained by chronopotentiometry at various current densities with 100%-iR compensation. For iR compensation, electrochemical impedance spectroscopy (EIS) was measured from 0.1 Hz to 100 kHz. The produced H<sub>2</sub>O<sub>2</sub> concentration was evaluated using the standard ceric sulfate (Ce(SO<sub>4</sub>)<sub>2</sub>) titration method, according to the following equation:



An aliquot of electrolyte was extracted after every chronopotentiometry test and added to 0.6 mM Ce(SO<sub>4</sub>)<sub>2</sub> in 0.5 M H<sub>2</sub>SO<sub>4</sub> titrant solution. The absorbance of the mixed solution was measured using UV-vis spectrophotometer (Cary100, Varian) at 319 nm. The amount of generated H<sub>2</sub>O<sub>2</sub> was calculated using the decrease in absorbance from original titrant solution. The faradaic efficiency of H<sub>2</sub>O<sub>2</sub> was calculated using the following equation:

$$\text{Faradaic efficiency}(\%) = \frac{n_{\text{H}_2\text{O}_2}(\text{mol}) \times 2 \times 96485(\text{Cmol}^{-1})}{I(\text{A}) \times t(\text{s})} \quad (7)$$

where  $n_{\text{H}_2\text{O}_2}$  indicates the total amount of produced H<sub>2</sub>O<sub>2</sub>,  $I$  is the applied current, and  $t$  is the time for the chronopotentiometry test.

## 2.8. Computational details

All density functional theory (DFT) calculations were performed using the Vienna Ab Initio Simulation Packages (VASP) [41] using the projector-augmented-wave (PAW) method [42] to describe the potential from the ionic core. For the exchange and correlation terms, generalized gradient approximation (GGA) of the Perdew-Burke-Ernzerhof (PBE) functional [43] including spin polarization were employed. A plane-wave energy cutoff of 500 eV and Monkhorst-Pack k-point meshes of 4 × 4 × 1 were used after an extensive convergence test. To prevent direct interaction between the original structure and its self-image, periodic boundary conditions (PBC) were applied with the vacuum separation distance set to 15 Å and 20 Å along the x- and z-directions, respectively.

All atom positions were fully optimized until the energy change was less than 1 × 10<sup>-6</sup> eV/cell and the force on each atom was less than 0.03 eV Å<sup>-1</sup>. To consider the van der Waals interaction between the reactants and graphene substrates, we additionally adopted Grimme's DFT-D3 method [44]. When we calculated the formation energies for four different components of BCO<sub>2</sub>, BC<sub>2</sub>O, BC<sub>3</sub>, B<sub>4</sub>C [32], we defined the

formation energy ( $E_f$ ) as following:

$$E_f = E_{B-doped\ Carbon} - (n_C\mu_C + n_B\mu_B + n_O\mu_O + n_H\mu_H) \quad (8)$$

where  $E_{B-doped\ Carbon}$  is the total energy of the B-doped carbon;  $\mu_C$  and  $\mu_B$  are the cohesive energies of the infinite graphene and  $\alpha$ -rhombohedral boron structures per atom respectively;  $\mu_O$  and  $\mu_H$  are the chemical potentials of nitrogen and hydrogen, identical to one-half of the binding energies of  $O_2$  and  $H_2$ , respectively;  $n_C$ ,  $n_B$ , and  $n_O$  are the numbers of carbon, boron, and doped oxygen atoms in the B-doped carbon;  $n_H$  is the number of the additionally introduced hydrogen atom in B-doped carbon edges only.

The porous carbon was simulated with three types of regions such as the graphene of basal plane, zigzag and armchair edges [34]. We adopted the VASPsol implicit solvation model ( $\epsilon = 78.5$ ) [45] to consider the solvation effects. The energetics of the ORR process was calculated based on the computational hydrogen electrode (CHE) model [46]. This model considers the chemical potential of  $(H^+ + e^-)$  to be

equal to the gas-phase  $\frac{1}{2} H_2$ . The catalytic activities of B-doped porous carbons were determined based on the  $^{*}OOH^*$  (\* denote a surface site) binding energy at each active site. Herein, the Gibbs free energy of  $^{*}OOH^*$  was calculated using the following equation,  $\Delta G = \Delta E_{DFT} + \Delta ZPE - T\Delta S + \Delta G_U$ , where  $\Delta E_{DFT}$  is the basis state energy from the DFT calculation,  $\Delta ZPE$  is the zero-point energy,  $T$  is the temperature (298.15 K)  $\Delta S$  is entropy, and  $\Delta G_U$  represents the effect of applied bias ( $-neU$ ).  $\Delta E$ ,  $\Delta ZPE$ , and  $T\Delta S$  values for reference gas molecules ( $H_2$ , and  $H_2O$ ) are taken from a previous study [47].

### 3. Results and discussion

#### 3.1. $CO_2$ conversion to B-doped porous carbon

The preparation of  $CO_2$ -derived BC, BPC and E-BPC is schematically illustrated in Fig. 1a. The E-BPC catalyst with high activity for the  $2e^-$  ORR was ultimately used in a flow reactor system to electrochemically produce  $H_2O_2$ . First, the pristine porous carbon (BC) was

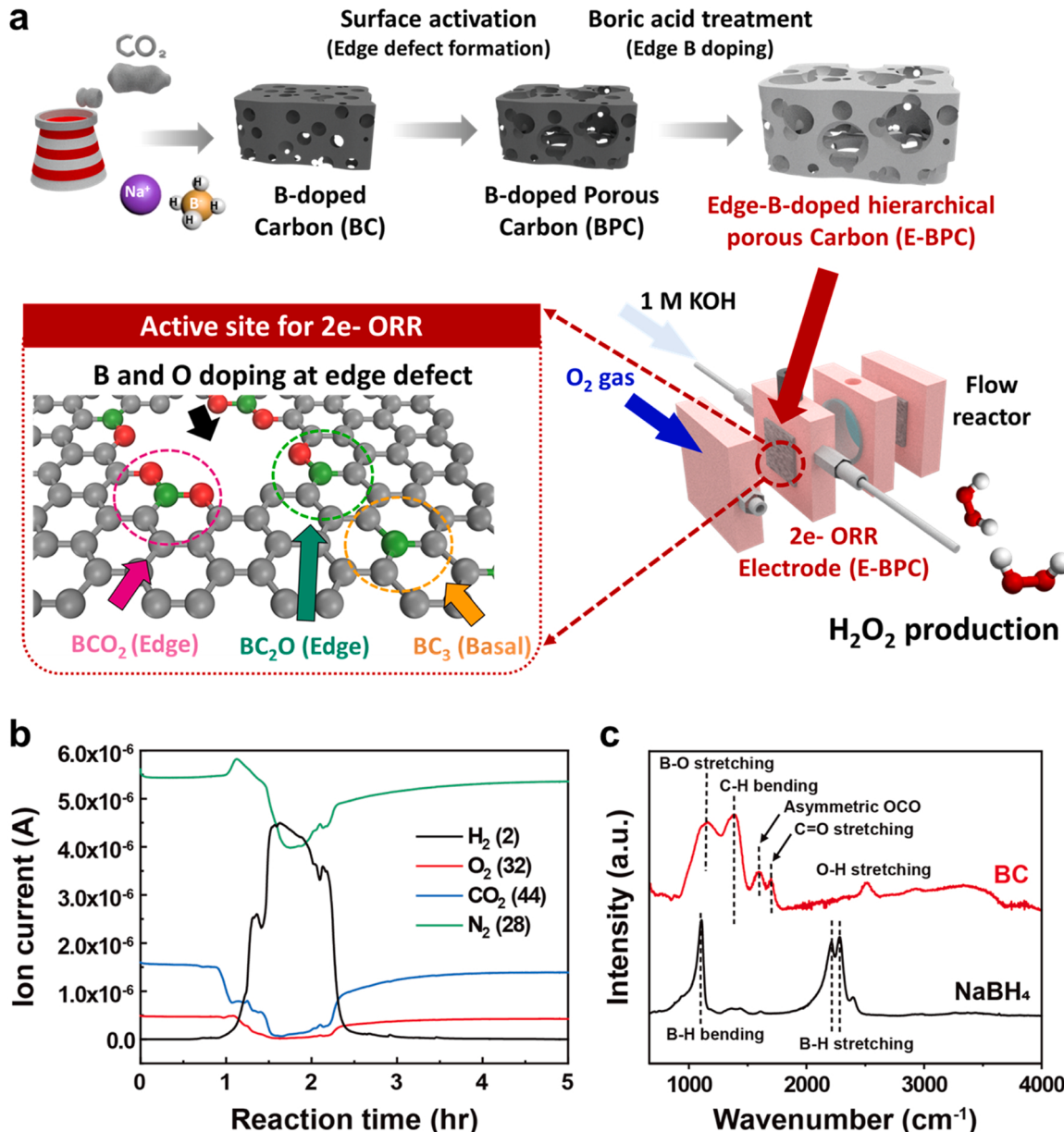


**Fig. 1.**  $CO_2$ -derived porous carbon materials for electrochemical  $H_2O_2$  production. (a) Schematic of this work; the gray, green, and red spheres represent carbon, boron, and oxygen atoms, respectively, (b) gas concentration changes during  $CO_2$  conversion process, and (c) FTIR spectra of  $NaBH_4$  and B-doped carbon (BC).

synthesized by converting  $\text{CO}_2$  using  $\text{NaBH}_4$  as a reducing agent. Since  $\text{CO}_2$  is a thermodynamically stable molecule with covalent double bonds between carbon and oxygen, thermal energy must generally be supplied to drive the desired transformation. The  $\text{NaBH}_4$  is an efficient reducing agent to convert  $\text{CO}_2$  at the relatively low temperature of 500–700 °C at atmospheric pressure. Usually, when using  $\text{NaBH}_4$  as a reducing agent (m.p. 400 °C), the  $\text{CO}_2$  reduction proceeds at temperatures higher than 400 °C [36,48]. In this work, to achieve both the  $\text{CO}_2$  conversion and surface activation via the  $\text{CO}_2$  activation expressed in Eq. (9), the reaction temperature was set to 700 °C. The  $\text{CO}_2$  activation effect of carbon can be explained by Boudouard reaction of Eq. 9, which needs high energy of more than 800 °C. However, The  $\text{CO}_2$  reactivity is highly dependent on the presence of alkali. Alkali metal can act as catalyst, the reactivity for the Boudouard reaction is much higher in the presence of alkali compared to the reaction only with pure carbon without alkali

metal [49]. In this work,  $\text{NaBH}_4$  start to decompose into alkali metal of sodium at around 500 °C, therefore, the Boudouard reaction is likely to occur at lower temperature of less than 800 °C.

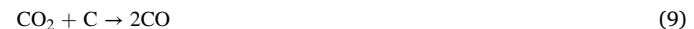


**Fig. 1b** shows the mass spectroscopy result obtained during a typical  $\text{CO}_2$  conversion process [50,51]. For  $\text{CO}_2$  conversion, a flue gas-motivated gas mixture of 85% of  $\text{N}_2$ , 10% of  $\text{CO}_2$ , and 5% of  $\text{O}_2$  was employed. The  $\text{H}_2$ ,  $\text{O}_2$ ,  $\text{CO}_2$ , and  $\text{N}_2$  profiles remain almost constant during the temperature-ramping step up to 400 °C, after which  $\text{CO}_2$  begins to decrease at the decomposition temperature of the  $\text{NaBH}_4$  while  $\text{H}_2$  begins to increase as it is emitted from the decomposition of  $\text{NaBH}_4$ . After the reaction was completed, in about ~1.5 hrs, the ionic current of the gases returned to its original value, which means that the powdery  $\text{NaBH}_4$  initially placed in the furnace reacted completely with  $\text{CO}_2$ ,

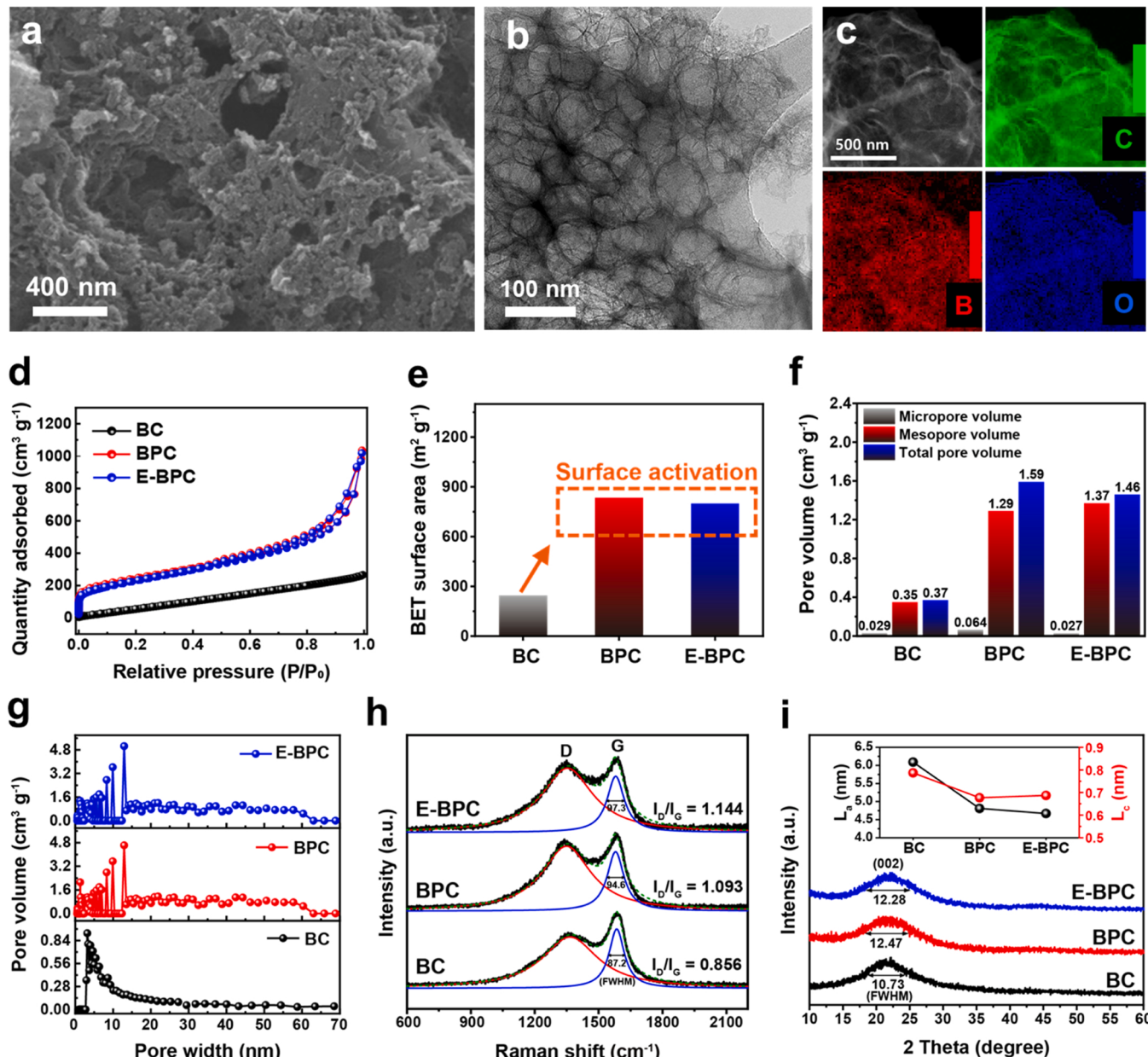


**Fig. 2.** Material characterizations of  $\text{CO}_2$ -derived carbon materials. (a) SEM, (b) TEM and (c) EELS elemental mapping of E-BPC, (d) Nitrogen adsorption-desorption isotherm plot, (e) BET surface area, (f) pore volume of micropores, mesopores and total pores, (g) pore size distribution, (h) Raman, and (i) XRD spectra of BC, BPC, and E-BPC. The inset in Fig. i shows the in-plane crystallite size ( $L_a$ ) calculated from Raman spectra and the crystallite height ( $L_c$ ) calculated from XRD of BC, BPC and E-BPC, respectively.

converting it to black BC powder highly doped with B (16.44 at% as shown in Table S1, Supplementary material). The FT-IR spectra shows that the B-H bending and B-H stretching modes of NaBH<sub>4</sub> at 1188, 2208, and 2288 cm<sup>-1</sup> disappeared for BC after the reaction of CO<sub>2</sub> and NaBH<sub>4</sub>, evolving new peaks corresponding to B-O stretching, C-O stretching, C-H bending, -OCO-, C=O stretching and O-H stretching at 891, 1164, 1395, 1586, 1702 and 2513 cm<sup>-1</sup>, respectively, as shown in Fig. 1c. This indicates that the powdery B-doped carbon material was successfully synthesized through the reduction of CO<sub>2</sub> by NaBH<sub>4</sub>, and B was naturally doped into the porous carbon materials (i.e., BC) from the B in NaBH<sub>4</sub> [52]. After that, BPC was obtained from the BC via a CO<sub>2</sub> activation process at 700 °C, which maximized the surface area and formed edge defects. Finally, E-BPC was obtained following boric acid treatment to add B dopant to the edge sites of BPC. This formed BCO<sub>2</sub> and BC<sub>2</sub>O doping configurations, in addition to the BC<sub>3</sub> configuration in the basal plane generated during the CO<sub>2</sub> conversion process.

### 3.2. Physicochemical properties of the CO<sub>2</sub>-derived B-doped porous carbon

To investigate the microstructure of the CO<sub>2</sub>-derived carbon materials, we carried out SEM, TEM, BET, XRD and Raman analyses. The hierarchical porous morphology of E-BPC was confirmed by SEM and TEM images as shown in Fig. 2a and b and the morphologies of BC and BPC were also confirmed by additional SEM and TEM microscopy (Fig. S1 and Fig. S2, Supplementary material). The pristine BC derived from CO<sub>2</sub> conversion exhibited a flake-like structure with several stacked flakes, the BPC had a more hierarchical pore structure due to the surface activation effect, which was similar to that of E-BPC. The high-resolution TEM images of E-BPC confirmed the amorphous character of E-BPC (Fig. S3, Supplementary material), which indicates that carbon materials derived from CO<sub>2</sub> conversion are closer to an amorphous carbon structure than the graphitic carbon structure. The EELS elemental mapping analysis of E-BPC was carried out as shown in Fig. 2c (also refer to Fig. S4, Supplementary material) and it was found that B dopants existed throughout the entire region of the carbon materials. This indicates the active sites for ORR exist uniformly within the catalysts.

The surface area and pore size distribution of the CO<sub>2</sub>-derived porous carbon materials were investigated by nitrogen (N<sub>2</sub>) adsorption and desorption measurements, as shown in Fig. 2d-g. The N<sub>2</sub> adsorption and desorption isotherms of BC derived from CO<sub>2</sub> reduction with NaBH<sub>4</sub> showed a type II isotherm with less developed micropore and mesopore structures. However, BPC and E-BPC showed highly porous structures of type IV isotherms with a large proportion of mesopores and a wide distribution of pore sizes (Fig. 2d). The BC exhibited a BET surface area of 244.4 m<sup>2</sup> g<sup>-1</sup> and total pore volume of 0.37 cm<sup>3</sup> g<sup>-1</sup>, while BPC and E-BPC showed increased BET surface areas of 834.6 and 797.7 m<sup>2</sup> g<sup>-1</sup> and total pore volumes of 1.59 and 1.46 cm<sup>3</sup> g<sup>-1</sup>, respectively (Fig. 2e-f). The noticeable change is that the significant increase in pore volume and surface area from BC to BPC and E-BPC arises from the effect of surface activation.

The formation mechanism of hierarchical pore structure of CO<sub>2</sub>-derived carbon with NaBH<sub>4</sub> can be divided into the three stages depending on the temperature range of low (200–300 °C), intermediate (~500 °C) and high temperature (>700 °C). At the low temperature of 200–300 °C, the reaction between NaBH<sub>4</sub> and CO<sub>2</sub> induces the product of sodium formatomethoxyborane [36]. At around 500 °C, however, NaBH<sub>4</sub> decomposes into Na and it reacts with CO<sub>2</sub>, which leads to the formation of porous carbon with micropores dominantly. BC, synthesized at 500 °C through the reaction between NaBH<sub>4</sub> and CO<sub>2</sub>, shows the pore size distribution mainly centered in the range of micropore, at around 4 nm. Finally, at the high temperature of 700 °C, the widening of micropores occurs, resulting in the formation of mesopore (2–50 nm) and macropores (>50 nm). In general, the CO<sub>2</sub> activation of carbon produces development of all the ranges of pore sizes of micropores,

mesopores, and macropores derived from the opening of micropores [53].

From the view point of catalyst utilization, we can expect that the increased porosity leads to an increase in the electroactive surface area available for catalytic reactions. Moreover, we found that E-BPC had a smaller surface area than that of BPC; the reduced surface is attributed to the decrease in micropores, from 0.064 cm<sup>3</sup> g<sup>-1</sup> for BPC to 0.027 cm<sup>3</sup> g<sup>-1</sup> for E-BPC and an increase in mesopores from 1.29 cm<sup>3</sup> g<sup>-1</sup> for the BPC to 1.37 cm<sup>3</sup> g<sup>-1</sup> for E-BPC (Fig. 2f-g). This might be attributed to a local structural rearrangement during the boric acid treatment at a high temperature of 800 °C. Generally, a reduction in the portion of micropores is beneficial for the electrocatalytic 2e<sup>-</sup> ORR reaction because micropores hinder the mass transport of reactants and products. Indeed, several studies have reported that micropores are detrimental for H<sub>2</sub>O<sub>2</sub> production [54,55]. The H<sub>2</sub>O<sub>2</sub> produced in mesopores can be easily released but the H<sub>2</sub>O<sub>2</sub> is trapped inside the micropores and then decomposes into H<sub>2</sub>O by disproportionation [55]. The pore size distribution in Fig. 2g indicates that the BPC and E-BPC have a hierarchical distribution of micropores along with increased volume of mesopores and macropores as diffusion path of H<sub>2</sub>O<sub>2</sub>, while BC has small volume of mesopores with a narrow pore size distribution centered at 3.4 nm. From this structural viewpoint, this can be expected to provide advantages for the 2e<sup>-</sup> ORR in the order of E-BPC, BPC, and BC.

In order to investigate the carbon structure and crystallite dimensions of the CO<sub>2</sub>-derived carbon materials, we employed Raman and XRD analyses. The Raman spectra in Fig. 2 h show the amorphous features of the BC, BPC and E-BPC as confirmed by TEM images (Fig. 2b and S3, Supplementary material). They showed two noticeable peaks at around 1340, 1580 cm<sup>-1</sup>, which are the D and G bands, showing the breathing and stretching modes of the sp<sup>2</sup> bonded carbon. Among them, the D bond is related to the edge-site defects on the crystallite [56]. The I<sub>D</sub>/I<sub>G</sub> ratio, which indicates the degree of carbon defects, was determined to be 0.856, 1.093, and 1.144 for BC, BPC, and E-BPC, respectively. As previously confirmed in the BET result, the rapid increase in surface area (244.4 m<sup>2</sup> g<sup>-1</sup> → 834.6 m<sup>2</sup> g<sup>-1</sup>) and pore volumes (0.37 cm<sup>3</sup> g<sup>-1</sup> → 1.46 cm<sup>3</sup> g<sup>-1</sup>) during the surface activation from BC to BPC increased the number of edge defects in the carbon, which led to an increase in the I<sub>D</sub>/I<sub>G</sub> ratio (0.856 → 1.093). Considering the rapid decrease in the B-doping concentration of BPC during the surface activation (16.44 at% → 0.38 at% as shown in Table S1), the main reason for the increased I<sub>D</sub>/I<sub>G</sub> ratio is closely related to the formation of edge defects on BPC. Meanwhile, the slight increase in the I<sub>D</sub>/I<sub>G</sub> ratio when changing from BPC to E-BPC is related to the additional B-doping of the edge defects during the boric acid treatment. The amount of B dopant was slightly increased in the process of transforming from the BPC to E-BPC, as confirmed by XPS, as shown in Table S1 (0.38 at% → 0.70 at %). For quantitative investigation of edge defects, Raman mapping was performed to obtain the I<sub>D</sub>/I<sub>G</sub> ratio in a wide range for BC, BPC, and E-BPC samples. As shown in Fig. S5, I<sub>D</sub>/I<sub>G</sub> ratio significantly increased after the surface activation process to obtain BPC from BC, and E-BPC also shows higher I<sub>D</sub>/I<sub>G</sub> ratio than BPC after the boric acid treatment. The increases in I<sub>D</sub>/I<sub>G</sub> ratio of BPC throughout the mapping region indicates that the pore activation evenly occurred and numerous edge sites for additional boron doping were created in this process. Besides, an increase of full width at half-maximum (FWHM) of the G peak indicates the increased number of edge defects [57]. The FWHM of G peak in Fig. 2 h increased from 87.2 to 94.6 in BPC after surface activation, also demonstrating the formation of edge defects. A more detailed analysis of the effect of the B-doping process on the edge-defects in BPC will be addressed in the XPS and DFT sections.

The X-ray diffraction (XRD) patterns of the B-doped carbon catalysts were measured, as shown in Fig. 2i. The BC, BPC, and E-BPC showed a broad (002) peak at around 22 degrees due to their amorphous nature, consistent with the Raman and TEM results. The stacking height (L<sub>c</sub>) of the crystallite (i.e., crystallite size in the direction perpendicular to graphene layers) can be calculated using the full width at half maximum

(FWHM) of the (002) peak and the Scherrer equation [58]. As a result, we found that the  $L_c$  of BPC (0.677 nm) and E-BPC (0.687 nm) was decreased compared to BC (0.787 nm). Likewise, the mean in-plain crystallite size ( $L_a$ ) of the carbon (i.e., lateral size of crystallite) was calculated using the Knight and White formula based on  $I_D/I_G$  ratio in Raman results [59], and the calculated  $L_a$  of BPC (4.81 nm) and E-BPC (4.67 nm) were also lower than that of BC (6.09 nm). That is, the decrease in crystallite size in the lateral and perpendicular directions means that more edge-defects were structurally created during the transformation from BC to BPC.

The carbon materials derived from  $\text{CO}_2$  conversion via the reaction between  $\text{NaBH}_4$  and  $\text{CO}_2$  in this work shows the amorphous feature of carbon from the result of TEM, Raman and XRD analysis. TEM image shows the amorphous feature of the  $\text{CO}_2$ -derived carbon without any crystallinity detected. Raman spectra shows the absence of 2D peak located at around  $2700 \text{ cm}^{-1}$ . It shows the feature of amorphous carbon with high intensity D peak and G peak at around  $1340$ ,  $1580 \text{ cm}^{-1}$ , respectively. D peak is attributed to the disordered aromatic structure of  $\text{sp}^3$  carbon and G peak is attributed to the stretching mode of  $\text{sp}^2$  bonded carbon. The 2D peak is the second order of D band without the need of defect in graphitized carbon. Finally, XRD result shows the broad feature of (002) and (101) peaks located at around  $23^\circ$  and  $44^\circ$ , respectively. Those peaks become sharper as the graphitization degree increases. The resulting  $\text{CO}_2$ -derived carbon showed broad feature of those peaks showing the amorphous carbon structure.

### 3.3. Active functional groups on the surface of the $\text{CO}_2$ -derived B-doped porous carbon

The surface atomic structure of the B dopants in  $\text{CO}_2$ -derived carbon materials was confirmed by high-resolution XPS and DFT calculations as shown in Fig. 3. The high-resolution XPS B 1 s spectra can be divided into four components of  $\text{B}_4\text{C}$ ,  $\text{BC}_3$ ,  $\text{BC}_2\text{O}$ , and  $\text{BCO}_2$  [60], which are located at around 187.8, 189.4, 191.2 and 192.8 eV, respectively

(Fig. 3a). In terms of B-doping concentration, the pristine BC showed the highest B contents of 16.44 at% compared to BPC (0.38 at%) and E-BPC (0.70 at%) (Fig. S6 and Table S1, Supplementary material). The boron contents are controllable depending on the reaction temperature of  $\text{CO}_2$  and  $\text{NaBH}_4$ . The boron contents obtained from the reaction at 500, 600, and 700 °C is 16.44, 3.36, and 0.38 at%, respectively (Table S1 in Supplementary materials). The sharp decreases in B-doping concentration from BC (16.44 at%) to BPC (0.38 at%) is thought to be due to the loss of B dopants resulting from structural and surface chemical changes during surface activation at high temperature under  $\text{CO}_2$ . Considering electron transport in carbon materials during electrochemical reactions, even though the B dopant does not significantly inhibit the electronic conductivity compared to O dopant, which localizes  $\pi$  electrons, too much B dopant (e.g., BC~16.44 at%) inevitably reduces the  $\text{sp}^2$  bonding of carbon, and this can decrease the electrical conductivity, resulting in lower catalytic performance. The slight increase in B-doping concentration from the BPC (0.38 at%) to E-BPC (0.70 at%) is due to the additional B-doping effect by the boric acid treatment at the edge-defects, generated by surface activation as mentioned above in the Raman and XRD results.

It is noteworthy that the proportion of the  $\text{BC}_3$ ,  $\text{BC}_2\text{O}$ , and  $\text{BCO}_2$  configurations (considered to be the main active sites for the  $2\text{e}^-$  ORR) gradually increased from BC to BPC and E-BPC, while the proportion of  $\text{B}_4\text{C}$  configuration (considered a less active site for the  $2\text{e}^-$  ORR) decreased. Note that the main active sites ( $\text{BC}_3$ ,  $\text{BC}_2\text{O}$ , and  $\text{BCO}_2$ ) and a less active site ( $\text{B}_4\text{C}$ ) mentioned here will be revealed by the DFT calculation and electrochemical results in the subsequent sections. More specifically, in the BC, the  $\text{B}_4\text{C}$  accounts for 50.1%, and  $\text{BC}_3$ ,  $\text{BC}_2\text{O}$ , and  $\text{BCO}_2$  account for 33.8%, 2.8%, and 13.3% respectively. The sum of the three portions, excluding  $\text{B}_4\text{C}$ , was 49.9% as shown in Fig. 3b. In contrast, in the BPC, the  $\text{B}_4\text{C}$  accounts for 37.4%, and  $\text{BC}_3$ ,  $\text{BC}_2\text{O}$ , and  $\text{BCO}_2$  account for 24.3%, 11.2%, and 27.1% respectively, and the sum of the three portions excluding  $\text{B}_4\text{C}$ , was 62.6%. In the E-BPC, the  $\text{B}_4\text{C}$  only accounts for 21.7%, and in  $\text{BC}_3$ ,  $\text{BC}_2\text{O}$ , and  $\text{BCO}_2$  accounts for 15.4%,

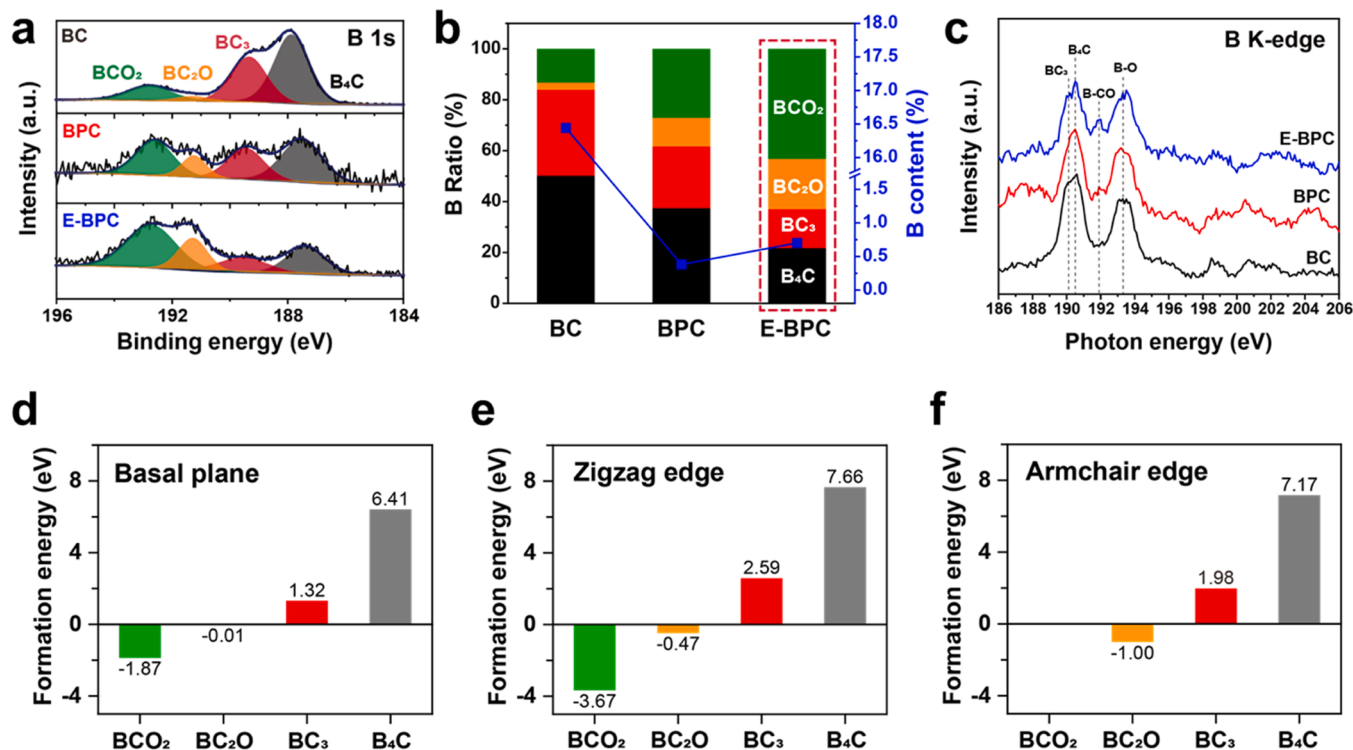


Fig. 3. Surface chemical analysis of B-doped carbon catalysts through XPS and DFT calculations. (a) B 1 s XPS spectra of BC, BPC and E-BPC. (b) Percentages of different B-doping configurations and B content in the BC, BPC and E-BPC. (c) NEXAFS B K-edge spectra of BC, BPC and E-BPC. Calculated formation energy for various B-doping configurations on three different regions of (d) carbon basal plane, (e) zigzag edge, and (f) armchair edge.

19.7%, and 43.2% respectively. The sum of three portions excluding  $B_4C$ , is 78.3%. Because the  $BC_3$ ,  $BC_2O$ , and  $BCO_2$  act as the main active sites of the  $2e^-$  ORR, the tendency could be responsible for the high activity of the E-BPC in the subsequent electrochemical evaluations.

To obtain further insight into the B-doping configuration in the carbon structures, near-edge X-ray adsorption fine structure (NEXAFS) measurements were performed. Fig. 3c shows the high-resolution boron K-edge NEXAFS spectra of BC, BPC, and E-BPC. All the samples exhibit four characteristic peaks at 190.1, 190.6, 192.0 and 193.5 eV. The former two peaks are associated with B-C bonds, which are assigned to the  $1s \rightarrow \pi^*$  transition at  $BC_3$  and  $B_4C$  bonding environment, respectively [61]. The latter two peaks are attributed to B-CO and B-O, confirming the existence of dual doping state of B and O [61,62]. Notably, the ratio of the B-O bond compared to the B-C bond increases in the order of  $BC < BPC < E-BPC$  and the intensity of the B-CO peak also increases in the same order, which is similar tendency as observed in the XPS results.

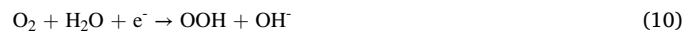
In addition to NEXAFS analysis, we also employed Time-of-flight secondary ion mass spectrometry (Tof-SIMS) analysis, because the depth of analysis is usually less than 1 nm, which is more surface-sensitive technique compared to XPS analysis with depth of 1–10 nm [63]. In Tof-SIMS mass spectrum, the boron-containing negative ions of  $B^-$ ,  $BO^-$ , and  $BO_2^-$  were identified at  $m/z = 11.0095$ , 27.0041, and 42.9962, respectively. The intensity of the resulting negative ions of  $B^-$  ( $m/z = 11.0095$ ) shows the trend of  $BPC < E-BPC < BC$  (Table S2 and Fig. S7 in Supplementary material), which is consistent with XPS analysis. To identify the relative mass ratio between  $B^-$  and oxygen containing B species of  $BO^-$  and  $BO_2^-$ , the intensity ratio of  $BO^-/B^-$  and  $BO_2^-/B^-$  were compared. The  $BO^-/B^-$  ratio increases in the order of  $BC < BPC < E-BPC$ . The  $BO_2^-/B^-$  ratio shows the similar trend of  $BC < BPC \approx E-BPC$ . The relative intensity ratio of  $BO^-/B^-$  is 46, 211, and 294 for BC, BPC and E-BPC, respectively. This shows that BPC synthesized at 700 °C induces more oxidized boron-containing species as a defect on the surface of carbon compared to BC and further boric acid-treated E-BPC shows more oxidized form of boron-containing species on the surface of edge sites compared to BPC. The original images of  $B^-$ ,  $BO^-$  and  $BO_2^-$  are shown in Supplementary material (Fig. S8). E-BPC shows homogeneous distribution of  $BO^-$  and  $BO_2^-$  species compared to BC and BPC. This result is consistent with XPS and NEXAFS analysis, showing more oxidized form of boron were detected for on the surface of E-BPC.

#### 3.4. The location of the active B-containing functional groups by DFT calculations

Although the quantitative analysis of various B-doping configurations in  $CO_2$ -derived carbon materials was investigated by XPS, as mentioned above, it was still unclear where the B-doping configurations were positioned. Because the  $2e^-$  ORR activity can change depending on the sites (e.g., basal plane or edge) of each doping configuration (e.g.,  $B_4C$ ,  $BC_3$ ,  $BC_2O$ , and  $BCO_2$ ) in the carbon structures, it is important to clarify the doping configuration structures in  $CO_2$ -derived carbon materials. To find plausible configurations of the B-C (e.g.,  $BC_3$  and  $B_4C$ ) and O-B-C (e.g.,  $BCO_2$  and  $BC_2O$ ) species in the  $CO_2$ -derived carbon materials, we investigated the thermodynamic stabilities of various carbon structures with B and O dopants using DFT calculations, in which we calculated their formation energies (Fig. 3d-f and Fig. S9 in Supplementary material). In modeling the porous carbon structures, we considered the  $BC_3$ ,  $B_4C$ ,  $BCO_2$ , and  $BC_2O$  configurations on the basal plane, zigzag edge, and armchair edge of graphene. According to the DFT calculations, the dual-doped configuration ( $BCO_2$  and  $BC_2O$ ) was thermodynamically more favorable than the single doped ones ( $BC_3$  and  $B_4C$ ), which supports the experimental results that the ratios of  $BC_3$  and  $B_4C$  decrease as the surface activation proceeds shown in Fig. 3b. In other words, the high formation energies of the  $B_4C$  and  $BC_3$  doping configurations indicate that the configurations are thermodynamically

unstable, which leads to a dramatic decrease in B-doping concentration (e.g.,  $BC \sim 16.44$  at% to  $BPC \sim 0.38$  at%) as well as a decrease in the  $B_4C$  and  $BC_3$  portion (e.g., 83.95 at% → 61.68 at%) from BC to BPC. The DFT calculations showed that the B-doping configurations on edge sites are more favorable than on the basal planes. In particular, the  $BCO_2$  and  $BC_2O$  species prefer positions on the zigzag and armchair edges, respectively.

In order to understand the origin of the superior catalytic activity of E-BPC, we calculated the free energy of  $^*OOH$  ( $\Delta G_{^*OOH}$ ) ( $^*$  denotes a surface site) on the B and O dual-doped carbon structures. It has been reported that the  $2e^-$  ORR activity is determined by the free energy of  $^*OOH$  intermediates [25,29,30], indicating that  $\Delta G_{^*OOH}$  can be a good descriptor for the  $2e^-$  ORR activity. For a catalyst with a weak tendency toward  $^*OOH$  adsorption,  $O_2$  activation (Eq. 10) is the potential limiting step (PDS) [64]:



On the other hand, for catalysts with strong  $^*OOH$  binding, there are two chemical reactions relevant to  $^*OOH$  desorption, as follows:

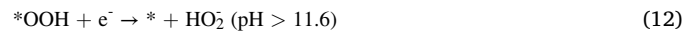
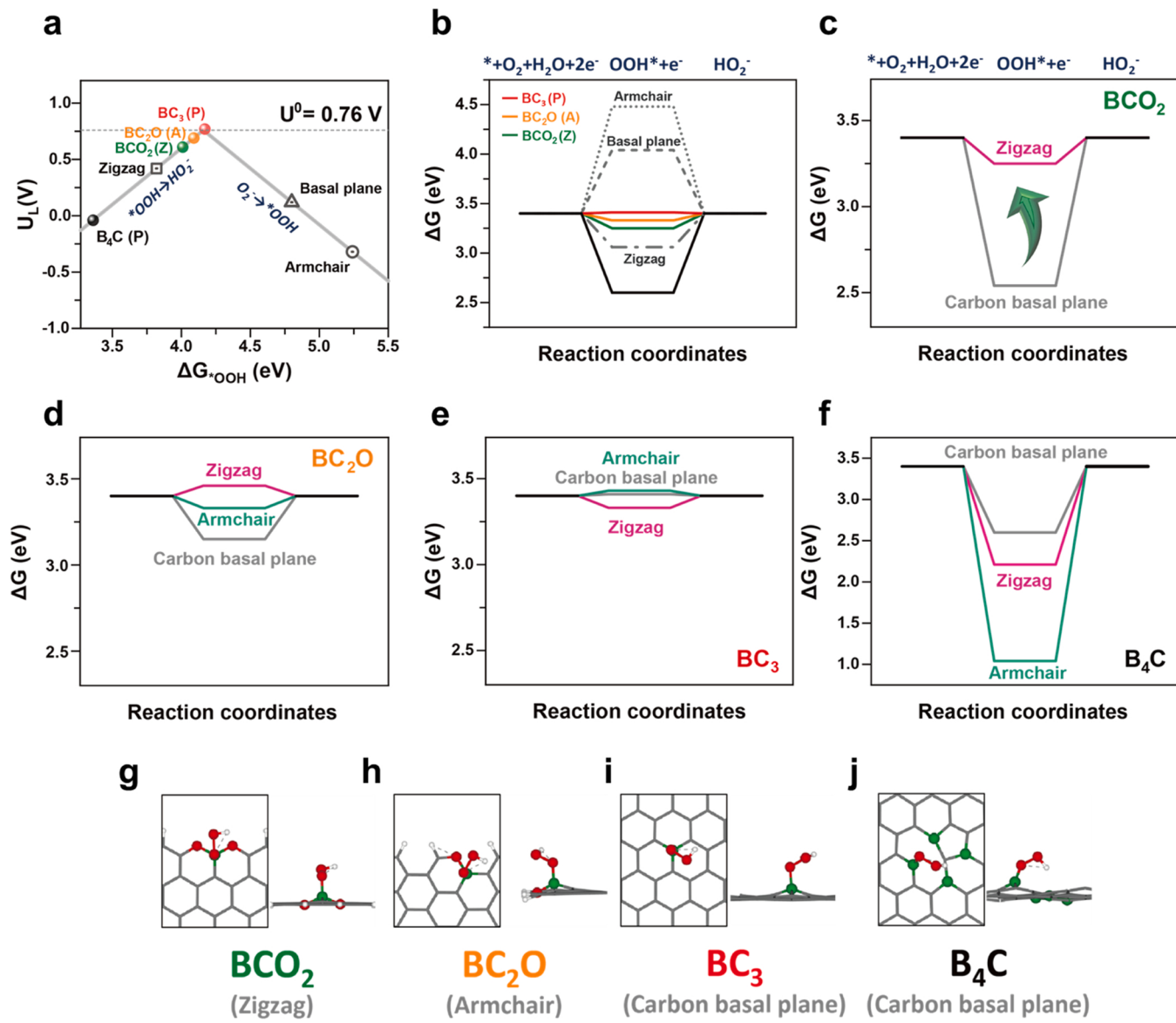


Fig. 4a shows a volcano plot of the catalytic activity for  $H_2O_2$  production by the  $2e^-$  ORR pathway in a base condition ( $pH = 13.5$ ). Herein, as the value of  $\Delta G_{^*OOH}$  approaches to 4.16 eV, it becomes closer to an ideal catalyst, with a zero overpotential which corresponds to the top of the ORR volcano plot, with a limiting potential ( $U_L$ ) of 0.7 V in  $pH < 11.6$ , and 0.76 V in  $pH > 11.6$  vs. RHE [29].

To clarify the active sites in the B-doped carbon structures for the  $2e^-$  ORR, we calculated the adsorption energies of  $^*OOH$  on various sites in the carbon structures by DFT calculations (Figs. S10 - S11 in Supplementary material). And it is found that the B-doping sites are most plausible as the active sites. Considering various configurations of the  $^*OOH$  intermediates on the carbon structures (Fig. S12, Supplementary material), the presence of  $BC_3$  ( $\Delta G_{^*OOH} = 4.17$  eV) on the carbon basal plane exhibited the lowest overpotential (0.01 eV), which agrees with the previous studies [32,35]. Moreover, the presence of  $BCO_2$  ( $\Delta G_{^*OOH} = 4.01$  eV) on the zigzag edge and  $BC_2O$  ( $\Delta G_{^*OOH} = 4.09$  eV) on the armchair edge showed a lower overpotential than the pristine carbon cases, while  $B_4C$  led to the highest overpotential (0.80 eV). Indeed, a Gibbs free energy diagram of the  $2e^-$  ORR at 0.76 V vs. RHE in Fig. 4b shows that the presence of  $BC_3$ ,  $BC_2O$ , and  $BCO_2$  leads to overpotentials lower than the pristine carbon. In particular, the  $\Delta G_{^*OOH}$  of  $BCO_2$  and  $BC_2O$  near edges in the B and O- dual doping system are positively higher than those on the basal planes (e.g., increases of 121.5% for  $BCO_2$  with the zigzag configuration and 104.1% for  $BC_2O$  with the armchair configuration) (Fig. 4c and d). However, when  $BC_3$  and  $B_4C$  are positioned at the carbon edges, they affect the  $2e^-$  ORR activity negatively (Fig. 4e and f). From the DFT calculations, it is evident that E-BPC samples with a high ratio of  $BC_3 + BC_2O + BCO_2$  exhibit superior catalytic activity for the  $2e^-$  ORR. In addition, we analyzed electronic structures of the carbon structures to clarify the origin on the high  $2e^-$  ORR activity (Figs. S13 and S14 in Supplementary material). Indeed, the presence of edges and the doping configuration can readily affect the  $2e^-$  ORR activity and the E-BPC mainly composed of  $BC_3$ ,  $BC_2O$ , and  $BCO_2$  can show excellent  $2e^-$  ORR performance. The detail discussion is included in the Supplementary material.

#### 3.5. $2e^-$ ORR performance of $CO_2$ -derived B-doped porous carbon

To evaluate the electrochemical  $H_2O_2$  production performance of  $CO_2$ -derived carbon materials, the  $2e^-$  ORR performance was evaluated using a rotating ring-disk electrode (RRDE) in a liquid half-cell. For a more accurate evaluation, the collection efficiency of the RRDE was



**Fig. 4.** DFT results of catalytic activities on dual B- and O-doped porous carbon. (a) Calculated catalytic activity volcanoes for  $H_2O_2$  production by the  $2e^-$  ORR pathway, with the limiting potential plotted as a function of  $\Delta G_{*OOH}$ . The black dashed line is the equilibrium potential of  $O_2/HO_2$ . (b-f) Gibbs free energy diagram of the  $2e^-$  ORR pathway to  $HO_2$  at the equilibrium potential of  $U_{O_2/HO_2} = 0.76$  V. RHE on four different dual B- and O-doping configurations of (c)  $BCO_2$ , (d)  $BC_2O$ , (e)  $BC_3$ , and (f)  $B_4C$ . Gibbs free energy diagram and each  $*OOH$  configuration of most advantageous  $2e^-$  ORR pathway in four different dual B- and O-doping configurations (g-j) were summarized in (b). Three different active site regions of carbon basal plane (grey), zigzag edge (pink), and armchair edge (coral) were considered separately.

experimentally calibrated and measured to be 0.25 (Fig. S15, Supplementary material). Fig. 5a shows the polarization curves of BC, BPC and E-BPC at 1600 rpm in  $O_2$ -saturated 0.1 M KOH solution. Among the  $CO_2$ -derived carbon materials, E-BPC showed the highest disk current (ORR) and ring current ( $H_2O_2$  oxidation), and the high  $H_2O_2$  selectivity (~88%) (Fig. 5b). The E-BPC and BPC showed significantly improved ORR activity and onset potential (defined as the potential at a ring current density of 0.15 mA cm<sup>-2</sup>) compared to the pristine BC. This is attributed to their B-doping configurations, which are favourable for the  $2e^-$  ORR as calculated in the DFT section, as well as their high surface area. In the CV curves of the electrochemical active surface area (ECSA) of the catalysts (Fig. S16, Supplementary material), the electrical double layer capacitances of the BC, BPC, and E-BPC were 1.01, 3.33, and 3.12 mF cm<sup>-2</sup>, respectively, which are consistent with the BET results. Namely, the ECSA of the catalyst is enlarged by about 3 times for BPC and E-BPC compared to BC, and this contributes to the increase in the

activity of the BPC and E-BPC. Meanwhile, our B-doped carbon catalysts also contain O dopants as shown in the XPS O 1 s spectra (Fig. S17 in Supplementary material). Even though the O dopant leads to high selectivity towards  $H_2O_2$ , there is a disadvantage such as low electrical conductivity due to the low crystallinity of carbon. In other words, a high concentration of O species over 16% in BC offers high selectivity, but in terms of activity (i.e., current density), it negatively affects  $2e^-$  ORR activity. In fact, there are no significant differences in O contents and configurations between BPC and E-BPC. Based on the similarity of BPC and E-BPC in O dopant contents and BET and electrochemical surface area, we calculated the ECSA-normalized disk and ring current densities (Fig. S18 in Supplementary material) by using the ECSA obtained from the CV curves (Fig. S16). Current densities per active site increased by about 47% for disk and 53% for ring at 0.5 V vs. RHE in E-BPC compared to BPC. This result indicates that the difference in ORR activity between BPC and E-BPC is mainly due to the difference in the B

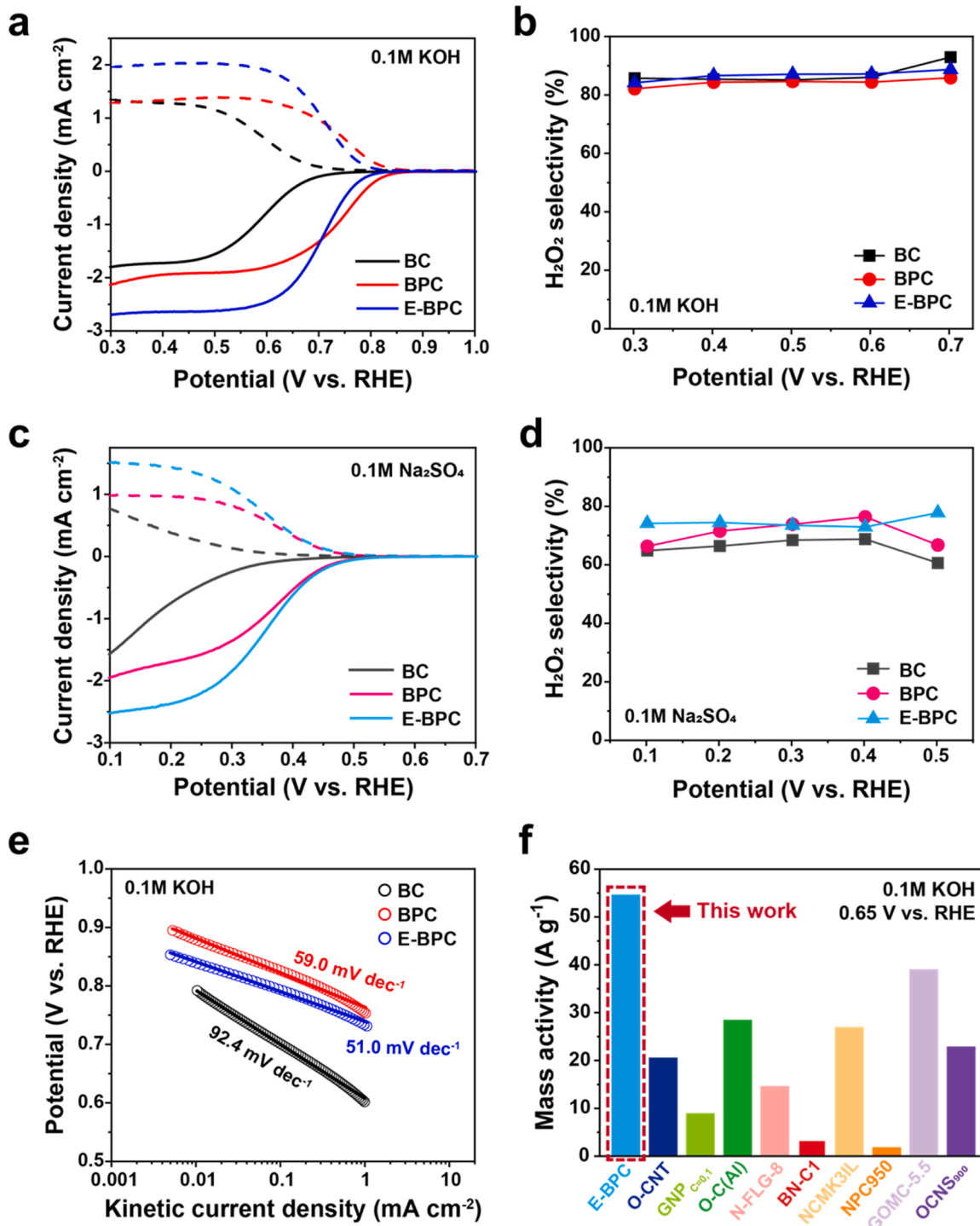


**Fig. 5.** Electrochemical performance of the catalysts for  $2\text{e}^-$  ORR. ORR performances of the  $\text{CO}_2$ -derived carbon materials by RRDE measured at 1600 rpm in (a)  $0.1 \text{ M KOH}$  and (c)  $0.1 \text{ M Na}_2\text{SO}_4$ .  $\text{H}_2\text{O}_2$  molar selectivity calculated from ORR curves in (b)  $0.1 \text{ M KOH}$  and (d)  $0.1 \text{ M Na}_2\text{SO}_4$ . (e) Tafel plots and (f) mass activity at  $0.65 \text{ V}$  vs. RHE of E-BPC in  $0.1 \text{ M KOH}$  compared to other metal-free catalysts reported in literatures.

dopant configuration and suggests that E-BPC has a large surface area and optimal edge B configuration with a moderate O dopant concentration which are advantageous to the high selectivity and activity towards  $2\text{e}^-$  ORR. From the RRDE results, we found that the selectivity of BC, BPC, and E-BPC is similarly high. This is because the energy barrier for the  $2\text{e}^-$  ORR shows no much difference depending on the B-doping configuration except for  $\text{B}_4\text{C}$ , as shown in the results of the DFT calculation (Fig. 4). That is, if the reaction occurs at the active site, the

selectivity for the  $2\text{e}^-$  pathway is expected to be similar, and it is considered that the activity varies depending on the number of active sites.

From the viewpoint of  $\text{H}_2\text{O}_2$  stability, it is also important to produce  $\text{H}_2\text{O}_2$  in neutral or acidic media. We evaluated  $2\text{e}^-$  ORR performance of B-doped carbon catalysts in a neutral electrolyte of  $0.1 \text{ M Na}_2\text{SO}_4$ , and E-BPC exhibited the highest ORR activity and selectivity of  $\sim 77\%$  (Fig. 5c and d), showing similar results as in alkaline electrolyte. Fig. 5e shows a

Tafel plot indicating the potential according to the kinetic current density in 0.1 M KOH. The Tafel slopes of the BC, BPC, and E-BPC are 92.4, 59.0, and 51.0 mV dec<sup>-1</sup>, which confirms that the E-BPC with the highest ORR activity has the fastest reaction kinetics. Electrochemical impedance spectroscopy (EIS) analysis was performed to further investigate the electrochemical behavior of the B-doped catalysts in the 2e<sup>-</sup> ORR environment. The Nyquist plot measured at 0.75 V vs. RHE

(Fig. S19, Supplementary material) shows that the E-BPC had the smallest semi-circle, and thus, the lowest charge transfer resistance ( $R_{ct}$ ). This result was obtained by fitting the Nyquist plot (refer to Table S3), and is highly consistent with the trend of the reaction kinetics in the Tafel plot. The mass activity was calculated from the kinetic current density (Fig. S20 and S21, Supplementary material), and the E-BPC showed the highest mass activity of 54.7 A g<sup>-1</sup> at 0.65 V vs. RHE in

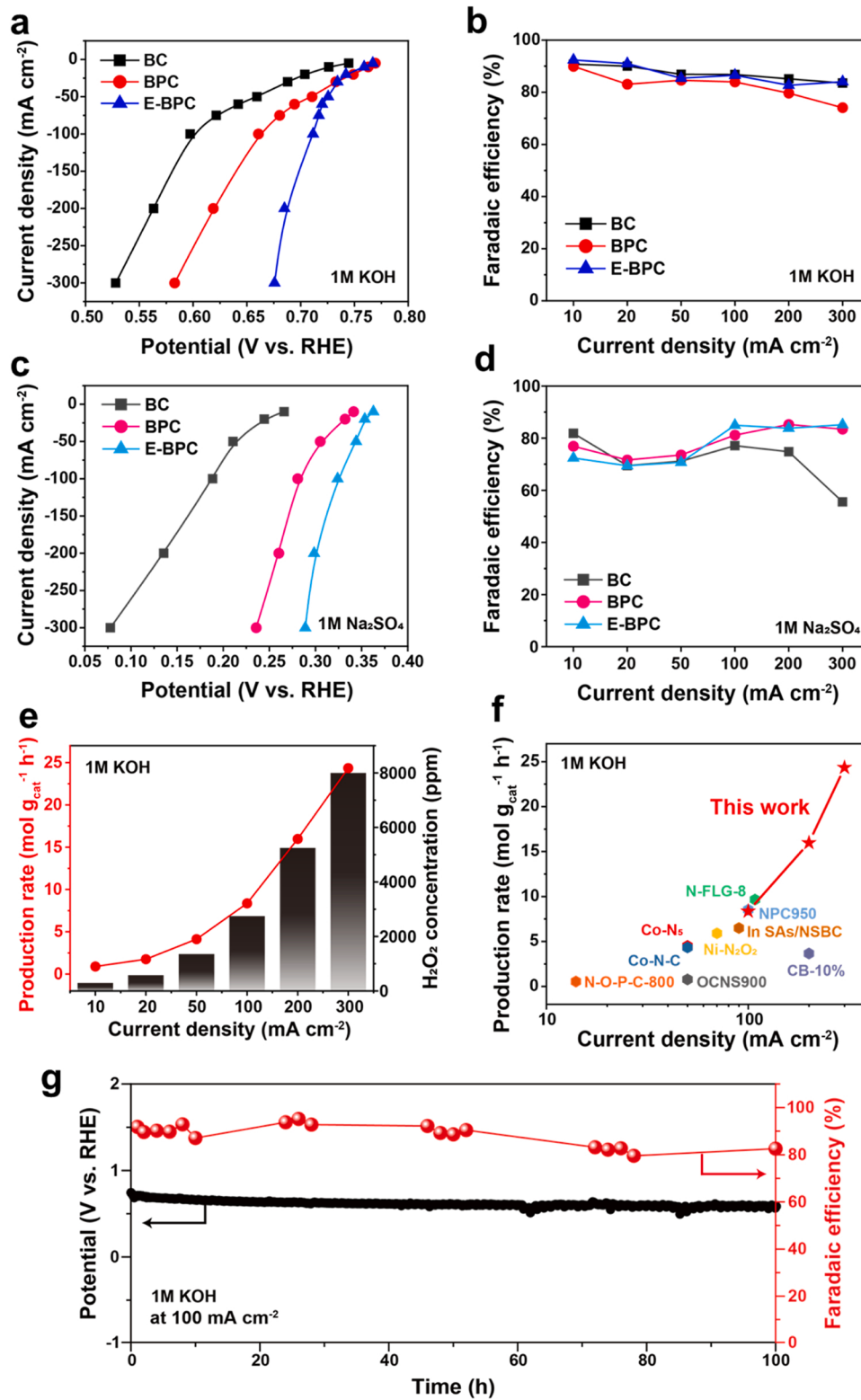


**Fig. 6.** Three-electrode flow-cell performance of the catalysts for electrochemical H<sub>2</sub>O<sub>2</sub> production. I-V curves under different current densities for BC, BPC, and E-BPC in (a) 1 M KOH and (c) 1 M Na<sub>2</sub>SO<sub>4</sub>. (b) Faradaic efficiency of BC, BPC, and E-BPC according to current densities in (b) 1 M KOH and (d) 1 M Na<sub>2</sub>SO<sub>4</sub>. (e) H<sub>2</sub>O<sub>2</sub> production rate and concentration of E-BPC. The amount of H<sub>2</sub>O<sub>2</sub> was measured in a separate fresh electrolyte at each current density. (f) Comparison of H<sub>2</sub>O<sub>2</sub> production rates with other reported works. (g) Stability test of E-BPC under 100 mA cm<sup>-2</sup> for 100 hrs.

0.1 M KOH and  $36.1 \text{ A g}^{-1}$  at 0.3 V vs. RHE in 0.1 M  $\text{Na}_2\text{SO}_4$ , respectively. In particular, as shown in Fig. 5f comparing the mass activity at 0.65 V vs. RHE in 0.1 M KOH in other reported studies, E-BPC showed the highest mass activity compared to metal-free catalysts reported to have high  $2e^-$  ORR activity so far (summarized in detail in Table S4) [29, 31, 54, 65–70]. In addition to the excellent catalytic activity, E-BPC showed excellent stability, maintaining a constant disk and ring current density for 12 h at 0.6 V vs. RHE (Fig. S22, Supplementary material).

### 3.6. The electrochemical production of hydrogen peroxide from the continuous flow cell

We conducted electrochemical  $\text{H}_2\text{O}_2$  production by  $2e^-$  ORR using a customized three-electrode flow cell based on the highly active E-BPC catalyst (Fig. S23, Supplementary material). The working electrode for the flow cell was fabricated by spray-coating the catalyst on a gas diffusion layer (GDL) covered with a microporous layer (MPL), as shown in the SEM image (Fig. S24, Supplementary material). Fig. 6a shows the I-V curves of the BC, BPC, and E-BPC measured in 1 M KOH with a flow rate of  $40 \text{ mL min}^{-1}$  and 20 sccm of  $\text{O}_2$  gas. The I-V curve was 100%-iR compensated manually and averaged after the 3 times repeated measurements. In the I-V curve, the ORR activity was high in the order of E-BPC, BPC, and BC, which was almost the same trend as the RRDE polarization curve. From the overpotential that was calculated based on the equilibrium potential of the  $2e^-$  ORR under the alkaline condition ( $\text{O}_2 + \text{H}_2\text{O} + 2e^- \rightarrow \text{HO}_2 + \text{OH}^-$ ,  $E^\circ = 0.76 \text{ V}$  vs. RHE), the E-BPC exhibited the lowest overpotential of 34 mV at  $50 \text{ mA cm}^{-2}$  (Fig. S25, Supplementary material). The difference in overpotential became more remarkable as the current density was rising. At the industrial-scale current density of  $300 \text{ mA cm}^{-2}$ , E-BPC showed an overpotential of only 84 mV, which is 148 mV less than that of pristine BC (232 mV). For comparison with oxidized carbon widely used in  $2e^-$  ORR, we additionally synthesized oxidized carbon black from commercial Vulcan XC 72 and evaluated  $\text{H}_2\text{O}_2$  production performance. As shown in I-V curve (Fig. S26 in Supplementary material), the oxidized carbon black indicates a significantly higher overpotential than E-BPC in current densities over  $200 \text{ mA cm}^{-2}$  and this gives rise to difficulty in practical applications. The faradaic efficiency of the catalyst according to the current density in Fig. 6b was calculated using the quantitative results of  $\text{H}_2\text{O}_2$  generated in the  $2e^-$  ORR, by cerium sulfate titration and UV-vis measurement (Fig. S27 and experimental section in Supplementary material). The E-BPC achieved the highest ORR activity and faradaic efficiency (~90%) simultaneously, as in the RRDE test result. As mentioned in RRDE test, the selectivity was almost similar between the samples (i.e., BC, BPC, and E-BPC) in RRDE test, but a slight difference occurred within about 5% of the Faraday efficiency between the samples in flow cell test. This is believed to be due to the operating conditions of high current density (hundreds of millamps per centimeter square) in the flow cells. At high current densities, a large mass transfer resistance occurs, which depends more on the structure of the electrode than on the surface properties. For this reason, although the RRDE test showed similar selectivity between samples, slight differences in Faradaic efficiency between samples can occur in flow cells operating at high current densities where mass transfer resistance occurs. In neutral electrolytes of 1 M  $\text{Na}_2\text{SO}_4$ , E-BPC also showed the highest ORR activity, faradaic efficiency (~85%) (Fig. 6c and d) and the lowest overpotential of 391 mV at  $300 \text{ mA cm}^{-2}$  based on the equilibrium potential of 0.68 V vs. RHE under neutral condition (Fig. S28 in Supplementary material). Fig. 6e shows the concentration of  $\text{H}_2\text{O}_2$  in the electrolyte as a function of current density, and the production rate, which is the amount of  $\text{H}_2\text{O}_2$  produced per hour and per mass of E-BPC. Based on  $40 \text{ mL}$  of 1 M KOH flowing through the reservoir and cell chamber, it was possible to produce up to 8000 ppm per hour at a current density of  $300 \text{ mA cm}^{-2}$ ; the maximum production rates were  $24.3 \text{ mol g}_{\text{cat}}^{-1} \text{ h}^{-1}$  and  $4.7 \text{ mmol cm}^{-2} \text{ h}^{-1}$  (Fig. S29, Supplementary material). Fig. 6f shows the reported production rate as a function of current density measured in the flow cell

setup (summarized in detail in Table S5). The E-BPC achieved a much higher  $\text{H}_2\text{O}_2$  production rate than the state-of-the-art oxidized carbons as well as metal single atom catalysts at the same current density [66, 68, 70–75]. Furthermore, the production rates of E-BPC in 1 M  $\text{Na}_2\text{SO}_4$  were  $23.8 \text{ mol g}_{\text{cat}}^{-1} \text{ h}^{-1}$  and  $4.76 \text{ mmol cm}^{-2} \text{ h}^{-1}$ , which are similarly high rates to that in 1 M KOH (Fig. S30 in Supplementary material). The energetically favourable B-doping configurations (e.g.,  $\text{BC}_3$ ,  $\text{BC}_2\text{O}$ , and  $\text{BCO}_2$ ) of the E-BPC as well as the hierarchical porous structure favourable for oxygen penetration and the diffusion of generated  $\text{H}_2\text{O}_2$  enabled the high-performance  $\text{H}_2\text{O}_2$  production, suitable for large-scale applications.

Lastly, we evaluated the electrochemical stability of E-BPC measured for 100 h at a current density of  $100 \text{ mA cm}^{-2}$  as shown in Fig. 6g. An aliquot of electrolyte was intermittently extracted during the reaction to measure the faradaic efficiency. After 100 h, the faradaic efficiency of the E-BPC remained at ~82% and the potential was 0.586 V vs. RHE. This indicates high stability while generating  $\text{H}_2\text{O}_2$  for 100 h without remarkable performance degradation. We also tested the stability in neutral media of 1 M  $\text{Na}_2\text{SO}_4$  to demonstrate stability under different pH conditions (Fig. S31 in Supplementary material), and E-BPC retains the faradaic efficiency over 80% after 24 h. The excellent stability of E-BPC is ascribed to the low overpotential (84 mV at  $300 \text{ mA cm}^{-2}$ ) by fast reaction kinetics, and the suppressed  $\text{H}_2\text{O}_2$  decomposition and free radical creation which are beneficial from the metal-free catalyst. Additionally, it was reported that defect sites in carbon are intrinsically stable to oxidation by free radicals [76, 77]. As shown in the DFT calculations (Fig. 3), more than half of the B-doping configuration of E-BPC is usually co-doped with O, and in this case, oxygenated B-doping configurations (i.e.,  $\text{BC}_2\text{O}$ , and  $\text{BCO}_2$ ) have a very stable formation energy. This leads to excellent electrochemical durability, because the active sites are well preserved, even during the long-term stability test. The high stability of oxygenated B-doping configurations was also confirmed by XPS and SEM images after the cell test as shown in Fig. S32 and S33 (Supplementary material). Hence, E-BPC exhibited not only high activity and selectivity but also excellent stability in electrochemical  $\text{H}_2\text{O}_2$  production.

## 4. Conclusions

We have demonstrated highly efficient and stable electrochemical  $\text{H}_2\text{O}_2$  production by the  $2e^-$  ORR using a  $\text{CO}_2$ -derived catalyst, E-BPC. The  $\text{CO}_2$  conversion process enabled the synthesis of hierarchical porous carbon materials, with controllable B-doping levels over a wide range and various doping configurations. Obtaining the high-performance E-BPC catalyst from greenhouse  $\text{CO}_2$  gases for the  $2e^-$  ORR is environmentally meaningful. Subsequently, by coupling material characterizations with DFT calculations, we found that edge-site defects were formed during the surface activation for BPC, and B dopants were incorporated into the edge-sites of E-BPC (e.g.,  $\text{BC}_2\text{O}$  and  $\text{BCO}_2$ ) during the boric acid treatment. The E-BPC obtained from  $\text{CO}_2$  gas exhibited the highest ORR activity ( $54.7 \text{ A g}^{-1}$  at 0.65 V vs. RHE) among reported metal-free catalytic materials and the highest  $\text{H}_2\text{O}_2$  production rate ( $24.3 \text{ mol g}_{\text{cat}}^{-1} \text{ h}^{-1}$ ) in a flow reactor system so far, surpassing reported value. In addition to excellent  $2e^-$  ORR characteristics, the long-term stability of E-BPC was also demonstrated in the electrochemical flow cell test, with no performance degradation after 100 h. We believe that this finding will be helpful for the design of B-doped carbon materials for electrochemical  $\text{H}_2\text{O}_2$  production through the  $2e^-$  ORR.

## CRediT authorship contribution statement

**Ayeong Byeon:** Conceptualization, Methodology, Investigation, Writing – original draft. **Jae Won Choi:** Conceptualization, Data curation, Investigation, Writing – original draft. **Hong Woo Lee:** Conceptualization, Data curation, Investigation, Writing – original draft. **Won Chan Yun:** Data curation, Investigation, Writing – review & editing.

**Wenjun Zhang:** Data curation, Investigation, Writing – review & editing. **Chang-Kyu Hwang:** Data curation, Investigation, Writing – review & editing. **Seung Yong Lee:** Data curation, Investigation, Writing – review & editing. **Sang Soo Han:** Writing – review & editing, Supervision, Project administration. **Jong Min Kim:** Writing – review & editing, Supervision, Project administration. **Jae W. Lee:** Writing – review & editing, Supervision, Project administration, Funding acquisition.

## Declaration of Competing Interest

The authors declare that they have no known competing financial interests or personal relationships that could have appeared to influence the work reported in this paper.

## Data Availability

No data was used for the research described in the article.

## Acknowledgements

A.B., J.W.C., and H.W.L. contributed equally to this work. The experimental work was supported by the KIST Institutional Program [grant number 2E31731]; the National Research Council of Science & Technology (NST) grant [grant number CPS21041-100]; and the ERC Program [grant number NRF-2022R1A5A1033719] and Basic Science Research Program by the National Research Foundation of Korea [grant number 2021R1A6A3A01087136]. The DFT calculation was supported by the Creative Materials Discovery Program [grant number 2016M3D1A1021141] and the National Center for Materials Research Data (NCMRD) through the National Research Foundation of Korea funded by the Ministry of Science and ICT [2021M3A7C2089739].

## Appendix A. Supporting information

Supplementary data associated with this article can be found in the online version at [doi:10.1016/j.apcatb.2023.122557](https://doi.org/10.1016/j.apcatb.2023.122557).

## References

- [1] H.S. Lim, D. Kang, J.W. Lee, Phase transition of  $\text{Fe}_2\text{O}_3$ – $\text{NiO}$  to  $\text{NiFe}_2\text{O}_4$  in perovskite catalytic particles for enhanced methane chemical looping reforming-decomposition with  $\text{CO}_2$  conversion, *Appl. Catal. B Environ.* 202 (2017) 175–183, <https://doi.org/10.1016/j.apcatb.2016.09.020>.
- [2] W. Liu, C. Zhang, J. Zhang, X. Huang, M. Song, J. Li, F. He, H. Yang, J. Zhang, D. Wang, Tuning the atomic configuration of Co-N-C electrocatalyst enables highly-selective  $\text{H}_2\text{O}_2$  production in acidic media, *Appl. Catal. B Environ.* 310 (2022), 121312, <https://doi.org/10.1016/j.apcatb.2022.121312>.
- [3] J.M. Kim, A. Jo, K.A. Lee, H.J. Han, Y.J. Kim, H.Y. Kim, G.R. Lee, M. Kim, Y. Park, Y.S. Kang, J. Jung, K.H. Chae, E. Lee, H.C. Ham, H. Ju, Y.S. Jung, J.Y. Kim, Conformation-modulated three-dimensional electrocatalysts for high-performance fuel cell electrodes, *Sci. Adv.* 7 (2022) eabe9083, <https://doi.org/10.1126/sciadv.abe9083>.
- [4] M. Lee, H. Lee, C. Seo, J. Lee, J.W. Lee, Enhanced energy efficiency and reduced  $\text{CO}_2$  emissions by hybrid heat integration in dimethyl carbonate production systems, *Sep. Purif. Technol.* 287 (2022), 120598, <https://doi.org/10.1016/j.seppur.2022.120598>.
- [5] E. Jung, H. Shin, B.-H. Lee, V. Efremov, S. Lee, H.S. Lee, J. Kim, W. Hooch Antink, S. Park, K.-S. Lee, S.-P. Cho, J.S. Yoo, Y.-E. Sung, T. Hyeon, Atomic-level tuning of Co-N-C catalyst for high-performance electrochemical  $\text{H}_2\text{O}_2$  production, *Nat. Mater.* 19 (2020) 436–442, <https://doi.org/10.1038/s41563-019-0571-5>.
- [6] E. Jung, H. Shin, W. Hooch Antink, Y.-E. Sung, T. Hyeon, Recent advances in electrochemical oxygen reduction to  $\text{H}_2\text{O}_2$ : catalyst and cell design, *ACS Energy Lett.* 5 (2020) 1881–1892, <https://doi.org/10.1021/acsenergylett.0c00812>.
- [7] W. Liu, J. Feng, R. Yin, Y. Ni, D. Zheng, W. Que, X. Niu, X. Dai, W. Shi, F. Wu, J. Yang, X. Cao, Tailoring oxygenated groups of monolithic cobalt-nitrogen-carbon frameworks for highly efficient hydrogen peroxide production in acidic media, *Chem. Eng. J.* 430 (2022), 132990, <https://doi.org/10.1016/j.cej.2021.132990>.
- [8] E. Miglbauer, P.J. Wójcik, E.D. Glowacki, Single-compartment hydrogen peroxide fuel cells with poly(3,4-ethylenedioxythiophene) cathodes, *Chem. Commun.* 54 (2018) 11873–11876, <https://doi.org/10.1039/C8CC06802J>.
- [9] A. Cervantes Trejo, I.D. Castañeda, A.C. Rodríguez, V.R. Andrade Carmona, M. del P.C. Mercado, L.S. Vale, M. Cruz, S. Barrero Castillero, L.C. Consuelo, M. Di Silvio, Hydrogen peroxide as an adjuvant therapy for COVID-19: a case series of patients and caregivers in the mexico city metropolitan area, *Evid. -Based Complement. Altern. Med.* 2021 (2021), 5592042, <https://doi.org/10.1155/2021/5592042>.
- [10] S.J. Freakley, Q. He, J.H. Harrhy, L. Lu, D.A. Crole, D.J. Morgan, E.N. Ntaijua, J. K. Edwards, A.F. Carley, A.Y. Borisevich, C.J. Kiely, G.J. Hutchings, Palladium-tin catalysts for the direct synthesis of  $\text{H}_2\text{O}_2$  with high selectivity, *Sci. (80. ).* 351 (2016) 965–968, <https://doi.org/10.1126/science.aad5705>.
- [11] X. Zhang, Y. Xia, C. Xia, H. Wang, Insights into practical-scale electrochemical  $\text{H}_2\text{O}_2$  synthesis, *Trends Chem.* 2 (2020) 942–953, <https://doi.org/10.1016/j.trechm.2020.07.007>.
- [12] A.T. Murray, S. Voskian, M. Schreier, T.A. Hatton, Y. Surendranath, Electrosynthesis of hydrogen peroxide by phase-transfer catalysis, *Joule* 3 (2019) 2942–2954, <https://doi.org/10.1016/j.joule.2019.09.019>.
- [13] X. Chuan, X. Yang, Z. Peng, F. Lei, W. Haotian, Direct electrosynthesis of pure aqueous  $\text{H}_2\text{O}_2$  solutions up to 20% by weight using a solid electrolyte, *Science.* 366 (2019) 226–231, <https://doi.org/10.1126/science.aa'y1844>.
- [14] G. Xia, Y. Tian, X. Yin, W. Yuan, X. Wu, Z. Yang, G. Yu, Y. Wang, M. Wu, Maximizing electrochemical hydrogen peroxide production from oxygen reduction with superaerophilic electrodes, *Appl. Catal. B Environ.* 299 (2021), 120655, <https://doi.org/10.1016/j.apcatb.2021.120655>.
- [15] J. Lee, S.W. Choi, S. Back, H. Jang, Y.J. Sa,  $\text{Pd}17\text{Se}15\text{-Pd}3\text{B}$  nanocoral electrocatalyst for selective oxygen reduction to hydrogen peroxide in near-neutral electrolyte, *Appl. Catal. B Environ.* 309 (2022), 121265, <https://doi.org/10.1016/j.apcatb.2022.121265>.
- [16] F. Sun, C. Yang, Z. Qu, W. Zhou, Y. Ding, J. Gao, G. Zhao, D. Xing, Y. Lu, Inexpensive activated coke electrocatalyst for high-efficiency hydrogen peroxide production: Coupling effects of amorphous carbon cluster and oxygen dopant, *Appl. Catal. B Environ.* 286 (2021), 119860, <https://doi.org/10.1016/j.apcatb.2020.119860>.
- [17] K. Dong, J. Liang, Y. Ren, Y. Wang, Z. Xu, L. Yue, T. Li, Q. Liu, Y. Luo, Y. Liu, S. Gao, M.S. Hamdy, Q. Li, D. Ma, X. Sun, Electrochemical two-electron  $\text{O}_2$  reduction reaction toward  $\text{H}_2\text{O}_2$  production: using cobalt porphyrin decorated carbon nanotubes as a nanohybrid catalyst, *J. Mater. Chem. A* 9 (2021) 26019–26027, <https://doi.org/10.1039/DITA07989A>.
- [18] L. Zhang, J. Liang, L. Yue, K. Dong, Z. Xu, T. Li, Q. Liu, Y. Luo, Y. Liu, S. Gao, A. M. Asiri, Q. Kong, X. Guo, X. Sun, CoTe nanoparticle-embedded N-doped hollow carbon polyhedron: an efficient catalyst for  $\text{H}_2\text{O}_2$  electrosynthesis in acidic media, *J. Mater. Chem. A* 9 (2021) 21703–21707, <https://doi.org/10.1039/DITA06313H>.
- [19] Q. Chen, C. Ma, S. Yan, J. Liang, K. Dong, Y. Luo, Q. Liu, T. Li, Y. Wang, L. Yue, B. Zheng, Y. Liu, S. Gao, Z. Jiang, W. Li, X. Sun, Greatly facilitated two-electron electroreduction of oxygen into hydrogen peroxide over  $\text{TiO}_2$  by Mn doping, *ACS Appl. Mater. Interfaces* 13 (2021) 46659–46664, <https://doi.org/10.1021/acsm.1c13307>.
- [20] K. Dong, J. Liang, Y. Wang, L. Zhang, Z. Xu, S. Sun, Y. Luo, T. Li, Q. Liu, N. Li, B. Tang, A.A. Alshehri, Q. Li, D. Ma, X. Sun, Conductive two-dimensional magnesium metal-organic frameworks for high-efficiency  $\text{O}_2$  electroreduction to  $\text{H}_2\text{O}_2$ , *ACS Catal.* 12 (2022) 6092–6099, <https://doi.org/10.1021/acscatal.2c00819>.
- [21] J. Zhang, A. Byeon, J.W. Lee, Boron-doped electrocatalysts derived from carbon dioxide, *J. Mater. Chem. A* 1 (2013) 8665–8671, <https://doi.org/10.1039/C3TA11248A>.
- [22] A. Byeon, H. Kim, J.H. Park, G.M. Kim, J.W. Lee, Highly active oxygen reduction reaction on Fe-nanoclustered hierarchical porous carbon derived from  $\text{CO}_2$ , *Chem. Commun.* 57 (2021) 13538–13541, <https://doi.org/10.1039/DCC05390F>.
- [23] J.M. Kim, J.-H. Kim, J. Kim, Y. Lim, Y. Kim, A. Alam, J. Lee, H. Ju, H.C. Ham, J. Y. Kim, Synergetic structural transformation of Pt electrocatalyst into advanced 3d architectures for hydrogen fuel cells, *Adv. Mater.* 32 (2020), 2002210, <https://doi.org/10.1002/adma.202002210>.
- [24] Q. Chang, P. Zhang, A.H.B. Mostaghimi, X. Zhao, S.R. Denny, J.H. Lee, H. Gao, Y. Zhang, H.L. Xin, S. Siahrostami, J.G. Chen, Z. Chen, Promoting  $\text{H}_2\text{O}_2$  production via 2-electron oxygen reduction by coordinating partially oxidized Pd with defect carbon, *Nat. Commun.* 11 (2020) 2178, <https://doi.org/10.1038/s41467-020-15843-3>.
- [25] S. Siahrostami, A. Verdaguér-Casadevall, M. Karamad, D. Deiana, P. Malacrida, B. Wickman, M. Escudero-Escribano, E.A. Paoli, R. Frydendal, T.W. Hansen, I. Chorkendorff, I.E.L.S. Stephens, I.E. Stephens, J. Rossmeisl, Enabling direct  $\text{H}_2\text{O}_2$  production through rational electrocatalyst design, *Nat. Mater.* 12 (2013) 1137–1143, <https://doi.org/10.1038/nmat3795>.
- [26] J.S. Jirkovský, M. Halasa, D.J. Schiffirrin, Kinetics of electrocatalytic reduction of oxygen and hydrogen peroxide on dispersed gold nanoparticles, *Phys. Chem. Chem. Phys.* 12 (2010) 8042–8053, <https://doi.org/10.1039/C002416C>.
- [27] S. Yang, J. Kim, Y.J. Tak, A. Soon, H. Lee, Single-atom catalyst of platinum supported on titanium nitride for selective electrochemical reactions, *Angew. Chem. Int. Ed.* 55 (2016) 2058–2062, <https://doi.org/10.1002/anie.201509241>.
- [28] J.S. Jirkovský, I. Panas, E. Ahlberg, M. Halasa, S. Romani, D.J. Schiffirrin, Single atom hot-spots at Au–Pd nanoalloys for electrocatalytic  $\text{H}_2\text{O}_2$  production, *J. Am. Chem. Soc.* 133 (2011) 19432–19441, <https://doi.org/10.1021/ja206477z>.
- [29] Z. Lu, G. Chen, S. Siahrostami, Z. Chen, K. Liu, J. Xie, L. Liao, T. Wu, D. Lin, Y. Liu, T.F. Jaramillo, J.K. Nørskov, Y. Cui, High-efficiency oxygen reduction to hydrogen peroxide catalysed by oxidized carbon materials, *Nat. Catal.* 1 (2018) 156–162, <https://doi.org/10.1038/s41929-017-0017-x>.
- [30] H.W. Kim, M.B. Ross, N. Kornienko, L. Zhang, J. Guo, P. Yang, B.D. McCloskey, Efficient hydrogen peroxide generation using reduced graphene oxide-based oxygen reduction electrocatalysts, *Nat. Catal.* 1 (2018) 282–290, <https://doi.org/10.1038/s41929-018-0044-2>.
- [31] G.-F. Han, F. Li, W. Zou, M. Karamad, J.-P. Jeon, S.-W. Kim, S.-J. Kim, Y. Bu, Z. Fu, Y. Lu, S. Siahrostami, J.-B. Baek, Building and identifying highly active oxygenated

groups in carbon materials for oxygen reduction to H<sub>2</sub>O<sub>2</sub>, Nat. Commun. 11 (2020) 2209, <https://doi.org/10.1038/s41467-020-15782-z>.

[32] Y. Xia, X. Zhao, C. Xia, Z.-Y. Wu, P. Zhu, J.Y. (Timothy) Kim, X. Bai, G. Gao, Y. Hu, J. Zhong, Y. Liu, H. Wang, Highly active and selective oxygen reduction to H<sub>2</sub>O<sub>2</sub> on boron-doped carbon for high production rates, Nat. Commun. 12 (2021) 4225, <https://doi.org/10.1038/s41467-021-24329-9>.

[33] R. Ma, G. Lin, Y. Zhou, Q. Liu, T. Zhang, G. Shan, M. Yang, J. Wang, A review of oxygen reduction mechanisms for metal-free carbon-based electrocatalysts, Npj Comput. Mater. 5 (2019) 78, <https://doi.org/10.1038/s41524-019-0210-3>.

[34] K. Dong, J. Liang, Y. Wang, Z. Xu, Q. Liu, Y. Luo, T. Li, L. Li, X. Shi, A.M. Asiri, Q. Li, D. Ma, X. Sun, Honeycomb carbon nanofibers: a superhydrophilic O<sub>2</sub>-trapping electrocatalyst enables ultrahigh mass activity for the two-electron oxygen reduction reaction, Angew. Chem. Int. Ed. 60 (2021) 10583–10587, <https://doi.org/10.1002/anie.202101880>.

[35] Y. Chang, J. Li, J. Ma, Y. Liu, R. Xing, Y. Wang, G. Zhang, Oxygenated boron-doped carbon via polymer dehalogenation as an electrocatalyst for high-efficiency O<sub>2</sub> reduction to H<sub>2</sub>O<sub>2</sub>, Sci. China Mater. 65 (2022) 1276–1284, <https://doi.org/10.1007/s40843-021-1891-2>.

[36] J. Zhang, J.W. Lee, Production of boron-doped porous carbon by the reaction of carbon dioxide with sodium borohydride at atmospheric pressure, Carbon 53 (2013) 216–221, <https://doi.org/10.1016/j.carbon.2012.10.051>.

[37] Y.K. Kim, J.H. Park, J.W. Lee, Facile nano-templated CO<sub>2</sub> conversion into highly interconnected hierarchical porous carbon for high-performance supercapacitor electrodes, Carbon 126 (2018) 215–224, <https://doi.org/10.1016/j.carbon.2017.10.020>.

[38] R. Liu, D. Wu, X. Feng, K. Müllen, Nitrogen-doped ordered mesoporous graphitic arrays with high electrocatalytic activity for oxygen reduction, Angew. Chem. Int. Ed. 49 (2010) 2565–2569, <https://doi.org/10.1002/anie.200907289>.

[39] S. Yang, X. Feng, X. Wang, K. Müllen, Graphene-based carbon nitride nanosheets as efficient metal-free electrocatalysts for oxygen reduction reactions, Angew. Chem. Int. Ed. 50 (2011) 5339–5343, <https://doi.org/10.1002/anie.201100170>.

[40] L. Yang, S. Jiang, Y. Zhao, L. Zhu, S. Chen, X. Wang, Q. Wu, J. Ma, Y. Ma, Z. Hu, Boron-doped carbon nanotubes as metal-free electrocatalysts for the oxygen reduction reaction, Angew. Chem. Int. Ed. Engl. 50 (2011) 7132–7135, <https://doi.org/10.1002/anie.201101287>.

[41] G. Kresse, J. Furthmüller, Efficiency of ab-initio total energy calculations for metals and semiconductors using a plane-wave basis set, Comput. Mater. Sci. 6 (1996) 15–50, [https://doi.org/10.1016/0927-0256\(96\)00008-0](https://doi.org/10.1016/0927-0256(96)00008-0).

[42] G. Kresse, D. Joubert, From ultrasoft pseudopotentials to the projector augmented-wave method, Phys. Rev. B. 59 (1999) 1758–1775, <https://doi.org/10.1103/PhysRevB.59.1758>.

[43] J.P. Perdew, K. Burke, Y. Wang, Generalized gradient approximation for the exchange-correlation hole of a many-electron system, Phys. Rev. B. Condens. Matter 54 (1996) 16533–16539, <https://doi.org/10.1103/physrevb.54.16533>.

[44] S. Grimme, J. Antony, S. Ehrlich, H. Krieg, A consistent and accurate ab initio parametrization of density functional dispersion correction (DFT-D) for the 94 elements H-Pu, J. Chem. Phys. 132 (2010), 154104, <https://doi.org/10.1063/1.3382344>.

[45] K. Mathew, R. Sundararaman, K. Letchworth-Weaver, T.A. Arias, R.G. Hennig, Implicit solvation model for density-functional study of nanocrystal surfaces and reaction pathways, J. Chem. Phys. 140 (2014) 84106, <https://doi.org/10.1063/1.4865107>.

[46] J.K. Nørskov, J. Rossmeisl, A.A. Logadottir, L. Lindqvist, J.R. Kitchin, T. Bligaard, H. Jónsson, Origin of the overpotential for oxygen reduction at a fuel-cell cathode, J. Phys. Chem. B. 108 (2004) 17886–17892, <https://doi.org/10.1021/JP047349J>.

[47] C. Tang, L. Chen, H. Li, L. Li, Y. Jiao, Y. Zheng, H. Xu, K. Davey, S.-Z. Qiao, Tailoring acidic oxygen reduction selectivity on single-atom catalysts via modification of first and second coordination spheres, J. Am. Chem. Soc. 143 (2021) 7819–7827, <https://doi.org/10.1021/jacs.1c03135>.

[48] G.M. Kim, W.-G. Lim, D. Kang, J.H. Park, H. Lee, J. Lee, J.W. Lee, Transformation of carbon dioxide into carbon nanotubes for enhanced ion transport and energy storage, Nanoscale 12 (2020) 7822–7833, <https://doi.org/10.1039/C9NR10552B>.

[49] M. Tangstad, J.P. Beukes, J. Steenkamp, E. Ringdalén, 14 - Coal-based reducing agents in ferroalloys and silicon production, in: I. Suárez-Ruiz, M.A. Diez, F.B.T.-N. T. in C.C. Rubiera (Eds.), Woodhead Publishing, 2019; pp. 405–438. <https://doi.org/10.1016/B978-0-08-102201-6.00014-5>.

[50] A. Byeon, W. Lee, G.M. Kim, J.W. Lee, Hierarchically porous heteroatom-doped carbon derived from flue gases for electrochemical energy storage, J. CO<sub>2</sub> Util. 16 (2016) 420–427, <https://doi.org/10.1016/j.jcou.2016.10.007>.

[51] S. Baik, B.L. Suh, A. Byeon, J. Kim, J.W. Lee, In-situ boron and nitrogen doping in flue gas derived carbon materials for enhanced oxygen reduction reaction, J. CO<sub>2</sub> Util. 20 (2021) 73–80, <https://doi.org/10.1016/j.jcou.2017.05.012>.

[52] A. Byeon, J. Park, S. Baik, Y. Jung, J.W. Lee, Effects of boron oxidation state on electrocatalytic activity of carbons synthesized from CO<sub>2</sub>, J. Mater. Chem. A. 3 (2015) 5843–5849, <https://doi.org/10.1039/C4TA0597D>.

[53] F. Rodríguez-Reinoso, M. Molina-Sabio, M.T. González, The use of steam and CO<sub>2</sub> as activating agents in the preparation of activated carbons, Carbon 33 (1995) 15–23, [https://doi.org/10.1016/0008-6223\(94\)00100-E](https://doi.org/10.1016/0008-6223(94)00100-E).

[54] Y. Sun, I. Sinev, W. Ju, A. Bergmann, S. Dresp, S. Kühl, C. Spöri, H. Schmies, H. Wang, D. Bernsmeyer, B. Paul, R. Schmack, R. Kraehnert, B. Roldan Cuenya, P. Strasser, Efficient electrochemical hydrogen peroxide production from molecular oxygen on nitrogen-doped mesoporous carbon catalysts, ACS Catal. 8 (2018) 2844–2856, <https://doi.org/10.1021/acscatal.7b03464>.

[55] J. Park, Y. Nabae, T. Hayakawa, M. Kakimoto, Highly selective two-electron oxygen reduction catalyzed by mesoporous nitrogen-doped carbon, ACS Catal. 4 (2014) 3749–3754, <https://doi.org/10.1021/cs5008206>.

[56] L. Castanheira, W.O. Silva, F.H.B. Lima, A. Crisci, L. Dubau, F. Maillard, Carbon corrosion in proton-exchange membrane fuel cells: effect of the carbon structure, the degradation protocol, and the gas atmosphere, ACS Catal. 5 (2015) 2184–2194, <https://doi.org/10.1021/cs501973j>.

[57] D. San Roman, D. Krishnamurthy, R. Garg, H. Hafiz, M. Lamparski, N.T. Nuhfer, V. Meunier, V. Viswanathan, T. Cohen-Karni, Engineering three-dimensional (3D) out-of-plane graphene edge sites for highly selective two-electron oxygen reduction electrocatalysis, ACS Catal. 10 (2020) 1993–2008, <https://doi.org/10.1021/acscatal.9b03919>.

[58] S. Zhang, Q. Liu, H. Zhang, R. Ma, K. Li, Y. Wu, B.J. Teppen, Structural order evaluation and structural evolution of coal derived natural graphite during graphitization, Carbon 157 (2020) 714–723, <https://doi.org/10.1016/j.carbon.2019.10.104>.

[59] D.S. Knight, W.B. White, Characterization of diamond films by Raman spectroscopy, J. Mater. Res. 4 (1989) 385–393, <https://doi.org/10.1557/JMR.1989.0385>.

[60] X. Yu, P. Han, Z. Wei, L. Huang, Z. Gu, S. Peng, J. Ma, G. Zheng, Boron-doped graphene for electrocatalytic N<sub>2</sub> reduction, Joule 2 (2018) 1610–1622, <https://doi.org/10.1016/j.joule.2018.06.007>.

[61] I. Caretti, R. Gago, J.M. Alberla, I. Jiménez, Boron carbides formed by coevaporation of B and C atoms: vapor reactivity, B<sub>x</sub>C<sub>1-x</sub> composition, and bonding structure, Phys. Rev. B. 77 (2008), 174109, <https://doi.org/10.1103/PhysRevB.77.174109>.

[62] O.V. Sedelnikova, Y.V. Fedoseeva, A.I. Romanenko, A.V. Gusel'nikov, O.Y. Vilkov, E.A. Maksimovskiy, D.S. Bychanok, P.P. Kuzhir, L.G. Bulusheva, A.V. Okotrub, Effect of boron and nitrogen additives on structure and transport properties of arc-produced carbon, Carbon 143 (2019) 660–668, <https://doi.org/10.1016/j.carbon.2018.11.071>.

[63] G.K. Saw, Tof-sims fragment pattern analysis of boron-doped chemical vapour deposition diamond, in: Multidiscip. Res. as Agent Chang. Ind. Revolut. 4.0, European Publisher, 2020, pp. 759–767.

[64] A. Kulkarni, S. Siahrostami, A. Patel, J.K. Nørskov, Understanding catalytic activity trends in the oxygen reduction reaction, Chem. Rev. 118 (2018) 2302–2312, <https://doi.org/10.1021/acs.chemrev.7b00488>.

[65] Q. Yang, W. Xu, S. Gong, G. Zheng, Z. Tian, Y. Wen, L. Peng, L. Zhang, Z. Lu, L. Chen, Atomically dispersed Lewis acid sites boost 2-electron oxygen reduction activity of carbon-based catalysts, Nat. Commun. 11 (2020) 5478, <https://doi.org/10.1038/s41467-020-19309-4>.

[66] L. Li, C. Tang, Y. Zheng, B. Xia, X. Zhou, H. Xu, S.-Z. Qiao, Tailoring selectivity of electrochemical hydrogen peroxide generation by tunable pyrrolic-nitrogen-carbon, Adv. Energy Mater. 10 (2020), 2000789, <https://doi.org/10.1002/aenm.202000789>.

[67] S. Chen, Z. Chen, S. Siahrostami, D. Higgins, D. Nordlund, D. Sokaras, T.R. Kim, Y. Liu, X. Yan, E. Nilsson, R. Sinclair, J.K. Nørskov, T.F. Jaramillo, Z. Bao, Designing boron nitride islands in carbon materials for efficient electrochemical synthesis of hydrogen peroxide, J. Am. Chem. Soc. 140 (2018) 7851–7859, <https://doi.org/10.1021/jacs.8b02798>.

[68] P. Cao, X. Quan, K. Zhao, X. Zhao, S. Chen, H. Yu, Durable and selective electrochemical H<sub>2</sub>O<sub>2</sub> synthesis under a large current enabled by the cathode with highly hydrophobic three-phase architecture, ACS Catal. 11 (2021) 13797–13808, <https://doi.org/10.1021/acscatal.1c03236>.

[69] J.S. Lim, J.H. Kim, J. Woo, D.S. Baek, K. Ihm, T.J. Shin, Y.J. Sa, S.H. Joo, Designing highly active nanoporous carbon H<sub>2</sub>O<sub>2</sub> production electrocatalysts through active site identification, Chem 7 (2021) 3114–3130, <https://doi.org/10.1016/j.chempr.2021.08.007>.

[70] S. Chen, T. Luo, K. Chen, Y. Lin, J. Fu, K. Liu, C. Cai, Q. Wang, H. Li, X. Li, J. Hu, H. Li, M. Zhu, M. Liu, Chemical identification of catalytically active sites on oxygen-doped carbon nanosheet to decipher the high activity for electro-synthesis hydrogen peroxide, Angew. Chem. Int. Ed. 60 (2021) 16607–16614, <https://doi.org/10.1002/anie.202104480>.

[71] Q. Zhao, Y. Wang, W.-H. Lai, F. Xiao, Y. Lyu, C. Liao, M. Shao, Approaching a high-rate and sustainable production of hydrogen peroxide: oxygen reduction on Co–N–C single-atom electrocatalysts in simulated seawater, Energy Environ. Sci. 14 (2021) 5444–5456, <https://doi.org/10.1039/DIEE00878A>.

[72] Y. Sun, L. Silivoli, N.R. Sahraie, W. Ju, J. Li, A. Zitolo, S. Li, A. Bagger, L. Arnarson, X. Wang, T. Moeller, D. Bernsmeyer, J. Rossmisl, F. Jaouen, P. Strasser, Activity-selectivity trends in the electrochemical production of hydrogen peroxide over single-site metal–nitrogen–carbon catalysts, J. Am. Chem. Soc. 141 (2019) 12372–12381, <https://doi.org/10.1021/jacs.9b05576>.

[73] Y. Wang, R. Shi, L. Shang, G.I.N. Waterhouse, J. Zhao, Q. Zhang, L. Gu, T. Zhang, High-efficiency oxygen reduction to hydrogen peroxide catalyzed by nickel single-atom catalysts with tetradentate N<sub>2</sub>O<sub>2</sub> coordination in a three-phase flow, Cell, Angew. Chem. Int. Ed. 59 (2020) 13057–13062, <https://doi.org/10.1002/anie.202004841>.

[74] C. Xia, Y. Xia, P. Zhu, L. Fan, H. Wang, Direct electrosynthesis of pure aqueous H<sub>2</sub>O<sub>2</sub> solutions up to 20% by weight using a solid electrolyte, Sci. (80-. ). 366 (2019) 226–231, <https://doi.org/10.1126/science.aay1844>.

[75] H.-X. Zhang, S.-C. Yang, Y.-L. Wang, J.-C. Xi, J.-C. Huang, J.-F. Li, P. Chen, R. Jia, Electrocatalyst derived from fungal hyphae and its excellent activity for

electrochemical production of hydrogen peroxide, *Electrochim. Acta* 308 (2019) 74–82, <https://doi.org/10.1016/j.electacta.2019.04.011>.

[76] Z. Chen, D. Higgins, A. Yu, L. Zhang, J. Zhang, A review on non-precious metal electrocatalysts for PEM fuel cells, *Energy Environ. Sci.* 4 (2011) 3167–3192, <https://doi.org/10.1039/C0EE00558D>.

[77] A. Byeon, W.C. Yun, J.M. Kim, J.W. Lee, Recent progress in heteroatom-doped carbon electrocatalysts for the two-electron oxygen reduction reaction, *Chem. Eng. J.* 456 (2023), 141042, <https://doi.org/10.1016/j.cej.2022.141042>.